Statistical Study of the Non-thermal Continuum Radiation Beaming Angle measured by the High Frequency Receiver on Van Allen Probes-A

S. A. Boardsen[1,2], E.-H. Kim[3], J. L. Green[4], C. Z. Cheng[3], I. H. Cairns[5], J. R. Johnson[6]

[1]NASA Goddard Space Flight Center, Greenbelt, Maryland, USA.

[2]Goddard Planetary Heliophysics Institute, University of Maryland in Baltimore, Maryland, USA.

[3]Princeton Plasma Physics Laboratory, Princeton University, Princeton, New Jersey, USA

[4]Space Science Endeavors LLC, Silver Spring, Maryland, USA

[5]Department of Physics, University of Sydney, Sydney, New South Wales, Australia

[6]Department of Engineering, Andrews University, Berrien Springs, Michigan, USA

Corresponding author: S. A. Boardsen (scott.a.boardsen@nasa.gov)

Key Points: (140 characters or less with no special characters or acronyms)

- Nonthermal continuum radiation beaming angles are calculated over the entire seven-year mission of Van Allen Probes-A.

- For frequencies ≲100 kHz the observed beaming angle pattern is consistent with the predictions from Linear Mode Conversion Theory.
- For frequencies ≳100 kHz another mechanism along with Linear Mode Conversion is needed.

Keywords: Linear Mode Conversion Theory, Nonthermal Continuum Radiation, Terrestrial Myriametric Radiation

Abstract

The nonthermal continuum radiation (NTC) beaming angle is computed over the entire Van Allen Probes A mission when the spacecraft was in the dawn sector. The conditions in the dawn sector are favorable for the wave vector to lie near/in the spacecraft's spin plan allowing a favorable estimate of the beaming angle, and the dawn sector is also advantageous in that previous studies show NTC occurrence to peak in this sector. We found that scatter plots, over the entire mission, of beaming angle versus magnetic latitude form a distinct inverted V pattern, with the apex at/near the magnetic equator. This pattern was sharpest for frequencies (f) $\lesssim$ 100 kHz. Using the NTC beaming formula from LMCT, we show that such an inverted V pattern is expected due to the large variation in the plasmapause location over the entire mission. The theoretical derived pattern qualitatively reproduces the observed pattern but not quantitatively. The lack of quantitative agreement is discussed and is attributed to several factors, one factor is off centered emissions from the radio window. The qualitative agreement strongly supports LMCT as being the dominant mechanism generating NTC for $f \lesssim$ 100 kHz. For $f \gtrsim$ 100 kHz the inverted V pattern becomes less distinct, and strong near equatorial beaming is observed. After considering contamination of our selections by left-handed polarized AKR, our study suggests that besides LMCT another unidentified NTC generation mechanism becomes important for $f \gtrsim$ 100 kHz.

Plain Language Summary

No summary given. Not required.

1. Introduction

Non-thermal continuum (NTC) radiation (also called terrestrial myriametric radiation) is free space ($f > f_{pe}$, f_{ce}, where f, f_{ce}, and f_{pe} are the wave, electron cyclotron, and plasma frequencies respectively) electromagnetic (EM) radiation for waves in the left-handed ordinary (L-O) mode observed in and near the Earth's magnetosphere and mainly outside the plasmasphere (Gurnett & Shaw, 1973; Gurnett 1975). NTC is believed to be emitted at strong density gradients chiefly at the equatorial plasmapause and is associated with electrostatic (ES) waves near the upper hybrid frequency (Gough et al., 1979; Kurth et al., 1981) and electron injections (Gough, 1982). This radiation can be produced over a broad frequency range from ~10 kHz to 100's of kHz and is roughly divided into two categories 1) trapped continuum where $f < f_{pe}$ at the magnetopause and escaping continuum where $f > f_{pe}$ at the magnetopause (Kurth et al., 1981). For $f \gtrsim 100$ kHz, escaping radiation is often called kilometric continuum (KC) radiation (Hashimoto et al., 1999; Green et al., 2002; Green et al., 2004; Hashimoto et al., 2005).

The widely accepted theory for the generation of NTC is linear mode conversion theory (LMCT) (Jones, 1976; Budden, 1980, Horne et al., 1989). In this theory electrostatic waves (ES) at frequencies of ~(n+½) f_{ce} (Kurth et al., 1979) are generated by electron loss cone distributions (Gough et al., 1979; Rönnmark & Christiansen, 1981) or weak ring-like features in the electron distribution (Sentman et al., 1979; Kurth et al., 1980) at/near the magnetic equator. As these ES waves propagate toward the higher density plasmapause, they convert into electromagnetic (EM) Z-mode waves on the same dispersion branch (e.g., Oya, 1971). Mode conversion from incoming Z-mode to the free space L-O wave mode radiation occurs at the radio window, where the Z-mode frequency matches the local electron plasma frequency. This process is depicted in Figure 4 of Jones (1980) and Figure 8 of Horne et al. (1989).

The key prediction of LMCT by Jones (1976) is that the mode-converted L-O mode waves can form two symmetrical beams relative to the magnetic equator as they propagate away from the equatorial plasmapause into lower densities outside the plasmasphere. The LMCT beaming formula is

$$\theta_B = \tan^{-1}\sqrt{\frac{f_{pe\_w}}{f_{ce\_w}}}. \qquad (1)$$

Here, θ_B is the beaming angle measured from the background magnetic field at the radio window $\boldsymbol{B}$ ($\boldsymbol{k} \parallel +\boldsymbol{B}$) or $-\boldsymbol{B}$ ($\boldsymbol{k} \parallel -\boldsymbol{B}$), $\boldsymbol{k}$ is a wave vector, f_{pe_w} and f_{ce_w} are the electron plasma and cyclotron frequencies at the window, respectively, and at the radio window, $f = f_{pe\_w}$ (Jones, 1980). The beaming formula holds at the window center where the waves experience no attenuation upon crossing. The window center is where the incoming Z-mode $\boldsymbol{k}$ is either parallel or anti-parallel to $\boldsymbol{B}$. Therefore, if Z-mode waves are propagating into the window from both the $+\boldsymbol{B}$ and $-\boldsymbol{B}$ directions, two symmetric L-O mode free space beams about the magnetic equator will be emitted from the radio window. We note that θ_B is the predicted asymptotic refraction (propagating away from the radio window as the index of refraction $\rightarrow 1$) of $\boldsymbol{k}$ away from the $\boldsymbol{B}$ direction as it propagates into the lower plasma density. For a typical plasmapause density gradient, this refraction of $\boldsymbol{k}$ from θ of 0° at the radio window center to ~ θ_B will occur over a radial distance of less than ~0.1 R_E, where R_E is Earth's radii (Jones, 1980; Horne, 1989). For off centered emission's the wave attenuation increases as the deviation of the beaming angle away from Θ_B increases (Budden, 1980). We note that studies often use the complement of Θ_B; $\lambda_B = \tan^{-1}(\sqrt{(f_{ce\_w} / f_{pe\_w})})$, which is a beaming angle between $\boldsymbol{k}$ and the magnetic equatorial plane.

The acceptance of the LMCT theory is based primarily on Jones et al. (1987), where Dynamics Explorer-1 observed two symmetrical NTC beams in magnetic latitude (λ_M) as the spacecraft transverses the magnetic equator. Other follow-up studies seeking to further verify the LMCT interpretation have either negative or mixed results (Morgan & Gurnett, 1991; Grimald et al., 2007) on the beaming angle predictions. Two multi-event/case studies of KC using GEOTAIL (Hashimoto et al., 2005) and IMAGE (Boardsen et al., 2008) spacecraft concluded that the LMCT beaming formula predicted too small (too large if complement of beam angle is used instead) of a beam angle Θ_B compared to the λ_M where the KC was observed.

In this paper, using the Van Allen Probes-A High Frequency Receiver (HFR) dataset over the entire mission, we perform a statistical study of the observed beaming angle Θ_B as a function of the spacecraft position and compare it with that predicted by LMCT. This paper is organized as follows. Section 2 describes the dataset and how Θ_B is computed. Section 3 explores the statistical set of Θ_B observations. Section 4 derives the theoretically predicted beaming angle using equation (1) as a function of satellite location, followed by a discussion and conclusion.

2. Remote Measurement of the Observed Beaming Angle

For observational studies cited in the introduction and this study, the electromagnetic radiation in the NTC frequency range was only sampled by one spin plane electric field antenna.

Therefore, the only approach to estimate the wave vector direction and the source beaming angle is from the analysis of the antenna's spin modulation curve. The modulation curve is (e.g., Kurth et al., 1975)

$$\left(\frac{E_i}{E_0}\right)^2 = \left(1 - \frac{m}{2}\right) - \frac{m}{2}\cos[2(\delta_i - \delta)], \qquad (2)$$

where E_i is the component of the vector electric field $\boldsymbol{E}$ measured by the spacecraft antenna at time step i, E_0 is the peak spin plane electric field, m is the modulation index, δ is the azimuthal angle of k in the spin plane, and δ_i is the antenna angle in the spin plane. At the time of the null ($\delta_i = \delta$) the antenna is aligned with the projection of $\boldsymbol{k}$ onto the spin plane because $\boldsymbol{k} \cdot \boldsymbol{E}$=0 for free space radiation. The modulation index m=1 corresponds to full modulation ($\boldsymbol{k}$ lies in the spin plane) and m =0 corresponds to no modulation.

In this study, we use the High Frequency Receiver (HFR) on the Van Allen Probes A spacecraft (Kletzing et al., 2013) for which only one spin plane electric field antenna is sampled by the receiver for a given time interval. Because we want $\boldsymbol{k}$ to lie nearly in the spin plane to estimate Θ_B, we need to analyze time intervals where the spin axis direction is nearly perpendicular to the radial direction of the Earth. The Van Allen Probes spin axis vector, which points to within ±28° of the Sun, is nearly perpendicular to the radial direction for MLTs around 6 MLT and 18 MLT. Continuum typically peaks around dawn (Gurnett and Frank, 1976). Fits were made only for periods when the angle between the spin axis and the radial position vector (Earth centered) was within $\pm 15^{o}$ of perpendicular orientation. In all, 6408 dawn sector time intervals were processed from 2012/10/15 to 2019/06/20. The onboard HFR spectral measurements consist of 82 logarithmically spaced frequencies ranging from 10 to 487 kHz. The cadence of the frequency sweeps is 0.5 s, which is small compared to the spin period of ~11 s. For each dawn sector time interval, spin modulation curve fits were performed on the HFR spectra dataset (Kletzing et al., 2022). Fits were performed for each frequency over a time range covering 1&1/2 spin periods (~33 measurements, ~17 s), staggering each time step by the one-time measurement between individual fits.

The analysis approach used in this study is that described in Morgan and Gurnett (1991). We rewrite the modulation equation (2) as

$$\rho_i(f) \ = \mathrm{C}_1 + \mathrm{C}_2 \cos(2\delta_i) + \mathrm{C}_3 \sin(2\delta_i) \qquad (3)$$

where $\rho_i(f)$ is the measured electric field power spectral density at frequency *f*, δ_i is and antenna spin phase angle at time step *i*, respectively, and C_1, C_2, and C_3 are the fit coefficients. Least squares fit of equation (3) are made over all data points within ±¾ of a spin period about the time of the center point *i*, solving for the fit coefficients C_1, C_2, and C_3. A five-point smoothing is performed on $\rho_i(f)$before fitting. The uncertainties of the fit coefficients ΔC_1, ΔC_2, and ΔC_3 are computed from the product of their variance with the diagonal elements of the covariance matrix (Bevington & Robinson, 1992). We found that the off-diagonal elements of this matrix are small relative to the diagonal elements, so the cross-correlations are set to zero when estimating the uncertainties in m, δ, and λ_0.

From C_1, C_2, C_3, ΔC_1, ΔC_2, and ΔC_3, one can compute m, δ, λ_0, and their uncertainties Δm, $\Delta\delta$, $\Delta\lambda_0$ as

$$m = 2\sqrt{\mathrm{C}_2{}^2 + \mathrm{C}_3{}^2}/(\mathrm{C}_1 + \sqrt{\mathrm{C}_2{}^2 + \mathrm{C}_3{}^2}), \quad (4)$$

$$\delta = \frac{1}{2}\tan^{-1}(\mathrm{C}_3/\mathrm{C}_2), \quad (5)$$

$$\cos^2(\lambda_0) = m. \quad (6)$$

In equation (6) λ_0 is the angle of ***k*** out of the spin plane. The uncertainties Δm, $\Delta\delta$, $\Delta\lambda_0$ are computed from square root of the square of differential form of equations (4-6) and setting the terms involving $\Delta C_1\Delta C_2$, $\Delta C_2\Delta C_3$, and $\Delta C_3\Delta C_1$, to zero due to their small cross-correlations. We note that Fainberg (1979) uses a different representation of the modulation curve $\left(\frac{E_i}{E_1}\right)^2 = 1 - m'\cos[2(\delta_i - \delta)]$, where E_1 is a constant and $0 \leq m' \leq 1$ is the modulation index, compared to equation (1) of this paper. The relation between the modulation index's is $m' = \frac{m}{2-m}$, λ_0 would be given by $cos^2(\lambda_0) = \frac{2m'}{1+m'}$. Both approaches are equally valid. The representation by Fainberg (1979) was used by Menietti et al. (1998) to estimate the direction of Jovian radio emissions.

Figure 1 is an example spin fit of the modulation curve for the frequency channel at 38.3 kHz. The fit parameters and their uncertainties are listed in the figure. For this fit, the uncertainty in δ is 3.6°, in 0.5 s between spectral measurements the antenna rotates through angle of ~16°. Using the spacecraft ephemeris (see Data Availability Statement) and the NAIF SPICE toolkit (Acton, 1996; Acton et al. 2017), the antenna orientation at the time of the null in modulation curve indicated by the blue curve in Figure 1 was computed. The antenna's unit vectors are in Solar Magnetic (SM) coordinates (***u***, ***v***, ***w***), where ***u*** and ***v*** are in the spin plane, and ***w*** is along the spin axis. For SM coordinates, the origin is Earth centered and the Z-axis (Z_{SM}) is parallel to the north magnetic pole. If the HFR is connected to $\boldsymbol{u}$ (or $\boldsymbol{v}$) antenna, then projection of wavevector $\boldsymbol{k}$ into the spin plane ($\hat{\boldsymbol{k}}_{sp}$) is aligned with $\boldsymbol{u}$ (or $\boldsymbol{v}$) to within a sign. The sign is chosen such that -$\boldsymbol{k}$ points Earthward (directed nearest to the Z_{SM} axis). The beaming angle Θ_B is estimated as an angle between $\hat{\boldsymbol{k}}_{sp}$ and $\boldsymbol{Z}_{\mathrm{SM}}$ if the spacecraft is in the northern hemisphere, and $\hat{\boldsymbol{k}}_{sp}$ and the -$\boldsymbol{Z}_{\mathrm{SM}}$ axis if the spacecraft is in the southern hemisphere.

We retain only Θ_B measurements for which a plasma density measurement (Kurth et al., 2015) was available in the plasma density data set (Kurth et al., 2020) for each fit time interval. The local plasma density is needed to compute the local plasma frequency f_{pe} to restrict the frequencies to the free space mode.

The 6408 processed time intervals were filtered for NTC emissions with strong modulation using the following criteria: $f > 1.2f_{\mathrm{pe}}$, m>0.6, $\Delta m/m < 0.2$, χ^2/χ_0^2<0.25. We use χ^2/χ_0^2 <0.25 in order that the sinusoidal fit is substantially improved over the constant offset fit given by χ_0^2. We also removed data during intervals judged to be saturated, this removed about 4% of the data points. Applying this filter reduces our set of Θ_B measurements to 1.6×10^7 frequency-time pixels. We found that the modulation index of type III radio bursts was consistently < 0.4, so contamination of our selections by these radio bursts is minimal.

Smoothing the signal will lower the modulation index because the dc component of the signal will not change, while the ac component will become smaller in amplitude. If the signal is a sine curve, the effect on m due to smoothing can be computed. The amplitude of a smoothed sine curve of unit amplitude is given by

$$b(\alpha, n) = \big(1 + 2\sin(n\alpha)\cos\big((n+1)\alpha\big) / \sin(\alpha)\big)/(2n+1), \qquad (7)$$

where 2n+1 is the amount of smoothing, and α is the angular increment between measurements. For five-point smoothing n = 2 and from the antenna rotation angle between measurements α = 2·16°, $b(\alpha, n) = 0.715$. The relation between m from the smooth sine curve and the modulation index m_c from the non-smoothed sine curve is

$$m_c = 2m/(2b(\alpha, n) + m\big(1 - b(\alpha, n)\big). \qquad (8)$$

The value m = 0.6 used as the lower limit in filtering the data gives m_c =0.750, which from equation (6) gives an out of spin plane angle estimate limit of 30° for the wave vector.

Frequency-time spectrograms of two orbital segments where the spin modulation curves were fitted are shown in Figures 2 and 3 for (a) spectral power density, (b) the modulation index m, (c) the chi-squared ratios χ^2/χ_0^2 and (d) selections that satisfied the selection criteria. The red line in Figure 3d at 53.6 kHz between 4.5 and 5 R_E are data points used in Figures 8, 9, &10. For f > 100 kHz strong contamination of the selections can occur. Figure 5 shows an extreme example of selected emissions 200 < f < 500 kHz interpreted to be heavily contaminated by L-O mode AKR when the spacecraft is at $\lambda_M > 10°$ and R > 5.3 R_E in dawn sector (MLT ~ 6). Green et al. (1977) using ray tracing showed that L-O mode can propagate from the source (dusk sector auroral field lines) across the polar cap and down to λ_M of about 10° on the dawn sector (unlike R-X mode AKR (Green et al., 1977; Xiao et al., 2016) which can easily propagate to the dusk sector equatorial inner magnetosphere). Looking at the ray tracing results of Green et al. (1977) this contamination will decrease as the magnetic latitude decreases in the dawn sector.

Histograms of the selected frequency-time pixels are presented in Figure 4 of (a) the radial distance (R), (b) the magnetic local time (MLT), (c) λ_M for $f < 100$ kHz, and (d) λ_M for $f > 100$ kHz. The y-axis is the number of selected frequency-time pixels per bin. Splitting the frequencies into those below and those above 100 kHz is because the emissions show a distinct change in the spatial characteristics as discussed in the next section. The magnetic latitude histograms are substantially different between $f < 100$ kHz (Figure 4(b)) and $f > 100$ kHz (Figure 4(d)). While the lower frequency case ($f < 100$kHz) shows a deep minimum at the magnetic equator, the higher frequency case ($f > 100$kHz) shows a strong peak at the magnetic equator. The former $f < 100$ kHz is quantitatively consistent with LMCT in the sense that the beaming is predicted to be directed out of the equatorial plane, while the later $f > 100$ kHz is not consistent with LMCT and is more consistent with the findings of Hashimoto et al. (2005) and Boardsen et al. (2008) where stronger equatorial beaming was suggested than that predicted by LMCT. The counts pick up moving away from the magnetic equator for $f > 100$ kHz in Figure 4(d), and we interpret this to be due to contamination of selections by L-O mode AKR which is predicted to become stronger as λ_M increases (Green et al. 1977).

3. Observed Beaming Angles Versus Magnetic Latitude

We explored scatter plots of the selections for each frequency as a function of various parameters against beaming angle (e.g., like radial distance, magnetic latitude, etc.). For scatter plots of magnetic latitude, the scatter exhibited an inverted V pattern with the apex at/near the magnetic, with the pattern clearer for frequencies below 100 kHz. Figure 5 shows scatter plots of Θ_B versus λ_M when spacecraft is located at a radial distance between 4 and 5 R_E ($4R_E < r < 5R_E$) for various frequency ranges, for a) f > 19 and < 51 kHz and b) f > 51 kHz and f < 100 kHz, c) f > 100 kHz and f < 147 kHz, and d) f >147 kHz and f < 500 kHz. Beyond the division at 100 kHz, the choice of frequency boundaries is arbitrary. For Figure 5(a-b), a distinct statistical inverted V pattern is observed about the magnetic equator. Note that the gap in detections in Figure 5(a) is consistent with the notch in the histogram in Figure 4(a). For Figure 5(c-d), an inverted V signature for $|\lambda_M| < 10°$ is observed in the running median, while for $|\lambda_M| > 10°$ we interpret the scatter to be strongly contaminated by L-O mode AKR.

Scatter plots of Θ_B versus MLAT for 5.5 $R_E < r <$ 6 R_E are shown in Figure 6(a-d). For the lower frequency radiations (f < 100kHz), an inverted V pattern is observed about the magnetic equator as shown in Figure 6(a-b), while no inverted V pattern is discernable for the higher frequencies as shown in Figure 6(b, d), which is interpreted to be due to L-O mode AKR contamination. Can the inverted V structure of beaming angles versus magnetic latitude observed in scatter plots covering the entire seven-year mission be explained in terms on LMCT? This will be explored in the next section.

4. Model Beaming Angle versus Spacecraft Position for Varying Plasmapause Location

If LMCT is the principal generation mechanism, what is the predicted statistical Θ_B pattern as a function of spacecraft position and detected NTC frequency f for a wide range of plasmapause locations? Figure 7(a) illustrates the meridian geometry used to interpret the results of our observational data analysis. The following assumptions are used: background magnetic field is an Earth center dipole anti-aligned with the Z_{SM} axis; the radio window is located at the equatorial plasmapause; the plasmapause is assumed to have local azimuthal symmetry; the emission is from the center of the window. Under these assumptions, the ray lies in the meridian plane. In Figure 7(a), the radio window (W) is located at an equatorial plasmapause at 2.5R_E, the blue line is the emitted NTC ray path for $f = f_{pe\_w}$ from W to the spacecraft (SC). Knowing the location of the radio window and spacecraft the beaming angle can be computed as

$$\tan\theta_B = \frac{\rho_{sc}-\rho_w}{z_{sc}}. \qquad (9)$$

The SC and W locations in the ρ -z plane is given by (ρ_{sc}, z_{sc}) and (ρ_w, 0) respectively, where $\rho = \sqrt{x^2 + y^2}$ in units of R_E. Using an Earth centered magnetic dipole f_{ce_w} is given as

$$f_{ce\_w} = \frac{870}{{\rho_w}^3}\ \text{Hz} \qquad (10)$$

for a dipole moment of 3.11x10^{-5} T. For this example, from the SC and W location $\theta_B = 47.9°$ from equation (9) and from equation (1&10) $f = f_{pe\_w} = 68.1$ kHz. For variable W location in equatorial radius (Figure 7b) and fixed f and SC r the solution of equations (1&9&10) results in an inverted V pattern for Θ_B versus λ_M (Figure 7c).

Figure 7(b) shows how Θ_B varies for different source locations *W* in the equatorial radial distance for four different NTC waves of f = 33.2, 53.6, 68.1, and 121.0 kHz. For example, for a sharp plasmapause at 2.5R_E, Θ_B is equal to 37.7°, 44.4°, 47.9° and 55.7° for the four frequencies, indicated by the black dots in Figure 7(b) and the latitudes at which the *SC* will observe them in Figure 7(c). The increase in Θ_B with increasing ρ_{SM} in Figure 7(b) is due to the increasing f_{pe_w}/f_{ce_w} ratio with increasing ρ_{SM} for fixed f_{pe_w}. Thus, as the magnetosphere becomes less active the geomagnetic K_p index decreases and the plasmapause moves outwards (e.g., Carpenter & Anderson, 1992; Moldwin et al., 2002) and Θ_B will increase.

Figure 7(c) presents the predicted model Θ_B for an SC radial position at 4.75 R_E as a function of magnetic latitude λ_M for plasmapause locations varying between 1.5 to 4.75 R_E. For a sharp plasmapause at 2.5R_E, the frequencies emitted at W (black dots in Figure 7(b) will be detected by the *SC* with a radial position R_{SC} = 4.75R_E at λ_M = ± 27.7°, ± 23.5°, ± 21.5°, and ± 17.0° (black dots in Figure 7c) for these four f respectively. For fixed radial position R_{SC} of the SC, as the plasmapause location varies due to changing geomagnetic conditions, an inverted V pattern of Θ_B versus λ_M with the apex located at the magnetic equator will be traced out as shown in Figure 7(c). The source location coincides with the virtual spacecraft position at the apex of the inverted V at $\lambda_M \to 0°$. As noted, because the beaming formula is asymptotic Θ_B does not equal the Z-mode angle of 0° at the radio window center.

Figure 8 shows a comparison of the observations with the model of Figure 7, for the same f and SC radial distances that lie within 4.5 < r < 5 R_E. A scatter plot of Θ_B versus λ_M is shown in Figures 8(a-d) for these four f. The error bars for Θ_B are plotted for 10 randomly selected points. To restrict the wave vector to lie closer to the spin plane, only points are plotted for which m >

0.8 (m_c = 0.96). The three blue curves are the theory curves for SC positions at r of 4.5, 4.75, and 5 R_E. Comparing the observations with the blue theory curves, one can see that the observations are qualitatively consistent with the model but are not always quantitatively consistent. With the disagreement of observed Θ_B with model the largest around λ_M of 0°, with the observations about 10° larger than the model Θ_B. Why quantitative agreement within measurement error is difficult and maybe impossible to obtain is discussed in the next section.

For f = 33.2, 53.6, 68.1 kHz a gap in the observations is observed straddling λ_M of 0° which would be expected from the off-equatorial beaming predicted by the theory. No such gap is observed for the large clustering of points for f = 120 kHz which is not consistent with the theory.

Can we detect a K_p dependence related to changing plasmapause location over the entire mission mentioned earlier in this section? Figure 8(e-h) plots K_p (Papitashvili and King, 2020) versus λ_M for the selections of Figure 8(a-d). The red lines are linear fits for $1 \leq K_p \leq 4$, and the number in each panel is the Spearman correlation coefficient. Unlike the linear fit, which is just a visual aid, this correlation is a nonlinear correlation which measures the degree that the data is monotonically related, a value of 1 indicates a strict monotonic increasing dependence, while a value of -1 indicates a strict monotonic decreasing dependence. The negative sign of the coefficients is consistent with the expected change in plasmapause position with Θ_B. However, the correlation is weak for f = 33.2 kHz with a value of -0.29, moderate for f = 53.6 and 68.1 kHz with values of -0.43 and -0.51 respectively, and for f = 120 kHz the value of -0.21 is poor. So below 100 kHz the correlation is moderate at best. We note that in the study of Moldwin et al.

(2002) the non-linear correlation for the overall dataset of radial plasmapause position versus K_p is 0.55 (see Figure 4 of that study), we should not expect to get a better correlation than this value since K_p is a fuzzy indicator of the plasmapause location. The uncertainty in the measurement of θ_B will also degrade the correlation.

5. Discussion

Qualitatively the observations for f < 100 kHz reproduce the inverted V structure of θ_B vs. λ_M predicted by LMCT theory for the large variation in plasmapause location over the duration of the mission. However, the error bars of many measurements do not encompass the model curve, with a systematic bias, especially for observations near the magnetic equator. We discuss why one might not expect quantitative agreement. Three major simplifications are used in our analysis: 1) the dawn sector plasmapause in our model is azimuthally symmetric, it has no azimuthal dependence. This allows one to use the simple model shown in Figure 7 for comparison with data. 2) The out of spin plane component is not used in the computation of θ_B, we justify this by using only data points with a large modulation index m > 0.6. 3) The emissions not from the center of the radio window need to be considered.

A radially directed plasmapause gradient used in this study is obviously an approximation. There are azimuthal variations in the plasmapause location as observed by the Extreme Ultraviolet Imager on the IMAGE spacecraft (e.g., Sandel et al., 2003). Here we make a back of the envelope estimate of how this could lead to a systematic offset of about 10°. To simplify the argument the measurement of azimuthal angles in SM coordinate system is shifted to the SC location. From Section 2, the lower limit used in the filter for the modulation index is m=0.8 (m_c = 0.96) which after correcting for smoothing gives a maximum out of plane angle for $\boldsymbol{k}$ of about 10.7°. Combining this angle with the requirement that the analyzed data segments are within ±15° of being radially directed gives an azimuthal angular range of ±26°. So, if the source is not radially outwards, but directed 26° in azimuth from the radial direction, the radial location of the azimuthally directed radio window of the source can be estimated. If the spacecraft is near the equator at a radial distance is 4.75 R_E and the plasmapause is 2.5 R_E (for a radially directed outward beam), using the law of cosines a radial distance of about 2.7 R_E for the radio window is computed for the azimuthally directed beam. Looking at Figure 7(b) the model beaming angle for a window at 3 R_E is about 5 degrees larger than the beaming angle for a window at 2.5 R_E and this will lead to a systematic offset. We note that the magnitude of the systematic offset will diminish as the radially directed window moves outward in radius, because the slope of the curve in Figure 7(b) decreases with increasing radius.

In principle, the modulation index m can be used to estimate the out of spin plane component of the wave vector direction. However, there are several factors that limit the interpretation of m and, therefore, its use in computing the out of spin plane component. 1) One factor is the variation of Z-mode radiation at the source over the time interval ~17 s of the fit. For example, the detected NTC in Figure 1 is not sinusoidal, and this could be due to variation of the Z-mode radiation at the source. The deviation of the observations from a sinusoidal curve limits the interpretation of m. 2) The smoothing of the data will lower the estimate of m, but this can somewhat be overcome by using the estimated correction given by equation (8). 3) The presence of background radiation can also degrade that interpretation of m, leading to a lowering of its actual value.

Many observations of NTC are not emissions from near the window center where the signal attenuation is near zero, but off centered where the signal experiences stronger attenuation. We will address attenuation using the f=53.6 kHz emissions from the orbit segment shown in Figure 2. The attenuation equation (23) of Budden (1980) will be used. This equation requires as input f_{ce_w}, $f=f_{pe\_w}$, S_1, S_2 and G; where S_1 is the asymptotic direction cosine of the emitted radiation along $\boldsymbol{B}$, $S_2=0$ is the direction cosine normal to both $\boldsymbol{B}$ and the density gradient, here $\boldsymbol{B}$ is taken to be perpendicular to the density gradient, and the scalar of the density gradient is G. To estimate the location of the window we will use the nearest plasmapause (Figure 9(a)) where f intersects f_{pe_w}, this occurs at 2016-07-12T18:37:06.482Z (red dots), where L=3.65, $|\lambda_M$ = 7.18°, MLT=7 h and f_{ce} = 18.34 kHz. Projecting this location using a dipole field line to the magnetic equator gives f_{ce_w} =17.04 kHz. The density variation is assumed to be in a function of only l-shell, and G is estimated to be -1971 m^{-4} from the gradient of the observed density variation with l-shell (Figure 9(b)).

The radiation pattern from the radio window is shown in Figure 9(c), -10 dB corresponds to a decade decrease the power spectral density. The window center is indicated by the black dot where the attenuation is 0 dB (100% transmission) and ϕ is azimuthal angle measured from the window location, a ϕ of 0° is directed outwards. We note that a spacecraft at ϕ of 30° will detect a 3 decade drop relative to the window center in the power spectral density. Using the same assumptions (ϕ =0°) as that used in Figure 7 for f=53.6 kHz, we show in Figure

9(d) that inverted V pattern persists as a function of dB for a plasmapause varying from 1.5 to 4.75 R_E. Including attenuation broadens the pattern in θ_B.

For the NTC beam at 53.6 kHz (Figure 2) the scatter plot of its observed θ_B versus time is shown in Figure 10(a). The black curve is the beaming angle θ_{BC} computed from the orbital position and the equatorial location of the plasmapause (Figure 9b). Based on the earlier discussions it is not expected that the scatter plot of beaming angle and the beaming angle curve should quantitatively agree, but they show similar trends with θ_B decreasing as the plasmapause is approached. A scatter plot of its phase space density versus time is shown in Figure 10b. Using θ_{BC} the attenuation (blue curve in Figure 10(b)) in dB on transmission through the radio window is computed using the parameters given in Figure 9(c). The shape of this curve is like the trend in the scatter; level near the window and decreasing moving toward larger radii, however the decrease with power and distance from the window is not factored in. The solid (dashed) curve is proportional to the product of the radio window attenuation times $1/{\rho_w}^2$ $(1/\rho_w)$, $1/{\rho_w}^2$would be a point source and $1/\rho_w$ would be a line source. Moving away from the plasmapause the power spectral density decreases by 3 orders of magnitude. Both the dotted-dashed and dotted curves drop off more rapidly than the observed scatter. This could be due to at least two factors 1) the true plasmapause of the radio window location is further outwards in radius than that of the proxy used (Figure 9b). 2) The power spectral density of the incoming Z mode does not peak at 0 or 180° but peaks at wave normal angles off 0 or 180 °, this would move the $1/{\rho_w}^2$ and $1/\rho_w$ curves to higher PSD moving outwards in radius. Figure 10(a, b) suggests that a significant fraction of the observations are emissions that are off centered from the window center.

For NTC with f > 100 kHz another mechanism along with LMCT must be occurring. At least three studies have suggested mechanisms for the direct generation of KC. Farrell (2001) suggested that weak energetic electron beams in a dense warm plasma (where $f_{pe} >> f_{ce}$) can directly generate L-O emission with propagation nearly perpendicular. Cheng (1975) has proposed a mechanism that will lead to near perpendicular beaming using electron ring distributions as the source. Horky and Omura (2019) performed electromagnetic simulations with an electron ring beam source in a warm plasma with a density gradient and suggested it can produce NTC, we believe their figures show near perpendicular beaming.

6 Conclusion

When the Earth's radial vector lay within ±15° of the Van Allen Probes spin plane (in the dawn sector), spin modulation curve fits were made to the 0.5 s cadence HFR frequency-time spectra data. These fits were performed at all f over the entire mission while in the dawn sector, which covers a vast range of plasmapause locations. To select nonthermal continuum radiation NTC, frequency-time pixels where selected using the following criteria: the frequency f was greater than 1.2 f_{pe}, the modulation index m was greater than 0.6, the relative error in m was small, and the ratio of the χ^2/χ_0^2 a sine wave to a constant offset fit was small. A m of 0.6 was chosen to ensure that the wave vector $\boldsymbol{k}$ lies with ~30° of the spin plane, given the limitation on the interpretation of m. The beaming angle Θ_B was estimated as the angle between the wave vector direction in the spin plane and the Z_{SM} axis.

Below 100 kHz, for a given f and radial distance bin, the observed pattern of Θ_B versus magnetic latitude λ_M forms an inverted pattern with the apex at the SM magnetic equator. Using the NTC beaming formula from LMCT, we show that such a pattern is predicted due to the large radial variation of the source equatorial plasmapause. Quantitatively the Θ_B has a systematic shift above the theory curve near that magnetic equator. A back of the envelope computation was performed to show that if the plasmapause is not azimuthally symmetric at the window one expects a systematic offset of 5-10° toward larger Θ_B. We discuss several factors that make the use of m in estimating of the out of spin plane component difficult. Two of the factors are smoothing of data before fitting and variation in the Z-mode intensity at the radio window over the fit interval. By taking attenuation into account (Budden, 1980), we showed that the model inverted V becomes broadened in beaming angle by of about 10° near the window center (Figure 9d) at -20 db. This suggests that attenuation could be the major factor contributing to the spread in beaming angle. These factors make achievement of quantitative agreement between observations and theory difficult, if not impossible.

We found (for $1 \leq K_p \leq 4$) a negative Spearman correlation coefficient for the 3 frequencies investigated below 100 kHz, one with a weak correlation value and two with moderate values. This trend is expected, because as K_p index decreases the plasmapause on average will move outwards and f_{ce} will decrease leading to a decrease Θ_B from theory. We conclude that these two observations, 1) the observed inverted V pattern of Θ_B vs λ_M and 2) the weak to moderate K_p dependence, highly suggest that LMCT is the dominant mechanism for the generation of NCT for $f < 100$ kHz.

For f >100 kHz, our selections become contaminated with L-O mode AKR, this contamination decreases for | λ_M | (< 10°). A partial inverted V is observed at the low end of this f range, and no reliable trend in K_p index is observed. Unlike emissions with f < 100 kHz, where the clustering of detections tends to lie off the magnetic equator consistent with beaming out the equatorial plane, these emissions are clustered around the magnetic equator. We conclude that LMCT can explain only a subset of these observations for f> 100 kHz and that another mechanism is also needed in this f range.

Acknowledgments

We acknowledge fruitful discussions and comments from Dr. William S. Kurth. The work for the study was funded by NASA Roses Grant 80HQTR18T0066. This work was also partly funded by NASA through the GPHI Cooperative Agreement NNG11PL02A and PHASER 80NSSC21M0180. This material is based upon work supported by the U.S. Department of Energy, Office of Science, Office of Fusion Energy Sciences under contract DE-AC02-09CH11466. Work at Princeton University is under National Aeronautics and Space Administration (NASA) Grants 80HQTR18T0066 and 80HQTR19T0076. Work at Andrews University is supported by NASA grants NNX16AQ87G, 80NSSC19K0270, 80NSSC19K0843, 80NSSC18K0835, 80NSSC20K0355, NNX17AI50G, 80HQTR18T0066, 80NSSC20K0704, 80NSSC18K1578, 80NSSC22K0515, and NSF grants AGS1832207, AGS1602855, and AGS2131013.

Data Availability Statement

For attitude calculations, the NAIF ICY toolkit was used, the ephemeris data required by the toolkit is at https://cdaweb.gsfc.nasa.gov/pub/data/rbsp/rbspa/ephemeris/. The dataset citation for the HFR spectral data is Kletzing, C. A. (2022a), for plasma density is Kurth et al. (2022), and the K_p index is Papitashvili and King, (2020). These datasets are available at the https://cdaweb.gsfc.nasa.gov.

References

Acton, C.H., "Ancillary Data Services of NASA's Navigation and Ancillary Information Facility;" Planetary and Space Science (1996), Vol. 44, No. 1, pp. 65-70; DOI 10.1016/0032-0633(95)00107-7

Acton, C., N. Bachman, B. Semenov, Edward Wright (2017), A look toward the future in the handling of space science mission geometry; Planetary and Space Science; DOI 10.1016/j.pss.2017.02.013

Bevington, P.R. & Robinson, D. 1992, *Data Reduction and Error Analysis for the Physical Sciences* (WCB/McGraw-Hill).

Boardsen, S. A., J. L. Green, and B.W. Reinisch (2008), Comparison of kilometric continuum latitudinal radiation patterns with linear mode conversion theory, *J. Geophys. Res.*, 113, A01,219, doi: 10.1029/2007JA012319.

Budden, K.G (1980), The theory of radio windows in the ionosphere and magnetosphere, *Journal of Atmospheric and Terrestrial Physics*, 42-3, https://doi.org/10.1016/0021-9169(80)90036-7

Carpenter, D. L., & Anderson, R. R. (1992). An ISEE/Whistler model of equatorial electron density in the magnetosphere. *Journal of Geophysical Research*, **97**(A2), 1097– 1108. https://doi.org/10.1029/91ja01548

Cheng, C. -Z. (1975) Ordinary electromagnetic mode instability, Journal of Plasma Physics, 13, pp 335-348, doi 10.1017/S002237780002609X

Fainberg, J. (1979), Technique to determine location of radio sources from measurements taken on spinning spacecraft , NASA Technical Memorandum 80598. https://ntrs.nasa.gov/citations/19800008000

Farrell, W. M. (2001), Direct generation of O-mode emission in a dense, warm plasma: Applications to interplanetary type II emissions and others in its class, *J. Geophys. Res.*, 106(A8), 15701– 15709, doi:10.1029/2000JA000156.

Gough, M. P., Christiansen, P., Martelli, G. & Gershumy, E. J. (1979) Interaction of electrostatic waves with warm electrons at the geomagnetic equator. *Nature* **279,** 515–517, doi:10.1038/279515a0

Gough, M.P. (1982) Non-thermal continuum emissions associated with electron injections: Remote plasmapause sounding, *Planetary and Space Science* **30** (7), 657-668, doi: https://doi.org/10.1016/0032-0633(82)90026-5.

Grimald, S., Décréau, P. M. E., Canu, P., Suraud, X., Vallières, X., Darrouzet, F., and Harvey, C. C. (2007), A quantitative test of Jones NTC beaming theory using CLUSTER constellation, Ann. Geophys., 25, 823–831, doi: 10.5194/angeo-25-823-2007.

Gurnett, D. A. (1975), The Earth as a radio source: The nonthermal continuum, *J. Geophys. Res.*, 80(19), 2751– 2763, doi:10.1029/JA080i019p02751.

Gurnett, D. A., and Green, J. L. (1978), On the polarization and origin of auroral kilometric radiation, *J. Geophys. Res.*, 83(A2), 689– 696, doi:10.1029/JA083iA02p00689.

Gurnett, D. A., and Frank, L. A. (1976), Continuum radiation associated with low-energy electrons in the outer radiation zone, *J. Geophys. Res.*, 81(22), 3875– 3885, doi:10.1029/JA081i022p03875.

Gurnett, D. A., and Shaw, R. R. (1973), Electromagnetic radiation trapped in the magnetosphere above the plasma frequency, *J. Geophys. Res.*, 78(34), 8136– 8149, doi:10.1029/JA078i034p08136.

Green, J. L., Gurnett, D. A., and Shawhan, S. D. (1977), The angular distribution of auroral kilometric radiation, *J. Geophys. Res.*, 82(13), 1825– 1838, doi:10.1029/JA082i013p01825.

Green, J. L., B. Sandel, S. Fung, D. Gallagher, and B. Reinisch (2002), On the origin of kilometric continuum, *J. Geophys. Res.*, 107, doi: 10.1029/2001JA000,193.

Green, J. L., Boardsen, S., Fung, S. F., Matsumoto, H., Hashimoto, K., Anderson, R. R., Sandel, B. R., and Reinisch, B. W. (2004), Association of kilometric continuum radiation with plasmaspheric structures, *J. Geophys. Res.*, 109, A03203, doi:10.1029/2003JA010093.

Hashimoto, K., Calvert, W., and Matsumoto, H. (1999), Kilometric continuum detected by Geotail, *J. Geophys. Res.*, 104(A12), 28645– 28656, doi:10.1029/1999JA900365.

Hashimoto, K., Anderson, R. R., Green, J. L., and Matsumoto, H. (2005), Source and propagation characteristics of kilometric continuum observed with multiple satellites, *J. Geophys. Res.*, 110, A09229, doi:10.1029/2004JA010729.

Horky, M. and Y. Omura (2019), Novel nonlinear mechanism of the generation of non-thermal continuum radiation, Physics of Plasmas **26**, 022904 (2019); https://doi.org/10.1063/1.5077094

Horne, R. B. (1989), Path-integrated growth of electrostatic waves: The generation of terrestrial myriametric radiation, *J. Geophys. Res.*, 94(A7), 8895– 8909, doi:10.1029/JA094iA07p08895.

Jones, D. (1976), Source of terrestrial non-thermal radiation *Nature* **260,** 686–689, https://doi.org/10.1038/260686a0

Jones, D. (1980), Latitudinal beaming of planetary radio emissions. *Nature* **288**, 225–229. https://doi.org/10.1038/288225a0

Jones, D., Calvert, W., Gurnett, D. A., & Huff, R. L. (1987), Observed beaming of terrestrial myriametric radiation. *Nature* **328,** 391–395. https://doi.org/10.1038/328391a0

Kletzing, C. A., et al. (2013), The Electric and Magnetic Field Instrument Suite and Integrated Science (EMFISIS) on RBSP, *Space Sci. Rev.*, 179, 127–181, doi:10.1007/s11214-013-9993-6.

Kletzing, C. A. (2022), Van Allen Probe A Single Axis AC Electric Field Spectra burst data [Data set]. NASA Space Physics Data Facility. https://doi.org/10.48322/18b2-kt74.

Kurth, W.S. (1982), Detailed observations of the source of terrestrial narrowband electromagnetic radiation. Geophys. Res. Lett., 9: 1341-1344. https://doi.org/10.1029/GL009i012p01341

Kurth, W. S., Baumback, M. M., and Gurnett, D. A. (1975), Direction-finding measurements of auroral kilometric radiation, *J. Geophys. Res.*, 80(19), 2764– 2770, doi:10.1029/JA080i019p02764.

Kurth, W.S., Frank, L.A., Ashour-Abdalla, M., Gurnett, D.A. and Burek, B.G. (1980), Observations of a free-energy source for intense electrostatic waves. Geophys. Res. Lett., 7: 293-296. https://doi.org/10.1029/GL007i005p00293

Kurth, W. S., Gurnett, D. A., and Anderson, R. R. (1981), Escaping nonthermal continuum radiation, *J. Geophys. Res.*, 86(A7), 5519– 5531, doi:10.1029/JA086iA07p05519.

Kurth, W. S., De Pascuale, S., Faden, J. B., Kletzing, C. A., Hospodarsky, G. B., Thaller, S. and Wygant, J. R. (2015), Electron densities inferred from plasma wave spectra obtained by the Waves instrument on Van Allen Probes. *J. Geophys. Res. Space Physics*, 120: 904– 914. doi: 10.1002/2014JA020857.

Kurth, W. S., S. De Pascuale, J. B. Faden, C. A. Kletzing, G. B. Hospodarsky, S. Thaller, and J. R. Wygant (2022). Van Allen Probe A Electric and Magnetic Field Instrument Suite and Integrated Science (EMFISIS) Density and other Parameters derived by digitizing Traces on Spectrograms, Level 4 (L4), 0.5 s Data [Data set]: RBSP-A_DENSITY_EMFISIS-L4. NASA Space Physics Data Facility. https://doi.org/10.48322/c4ha-xj50.

Menietti, J. D., Gurnett, D. A., Kurth, W. S., Groene, J. B., and Granroth, L. J. (1998), Galileo direction finding of Jovian radio emissions, *J. Geophys. Res.*, 103(E9), 20001– 20010, doi:10.1029/97JE03555.

Moldwin, M. B., Downward, L., Rassoul, H. K., Amin, R., & Anderson, R. R. (2002). A new model of the location of the plasmapause: CRRES results. *Journal of Geophysical Research*, **107**(A11). SMP1-9–SMP2-9. https://doi.org/10.1029/2001ja009211

Morgan, D. D., and D. A. Gurnett (1991), The source location and beaming of terrestrial continuum radiation, J. Geophy. Res., 96, 9595. https://doi.org/10.1029/91JA00314

Papitashvili, N. E., & and King, J. H. (2020), OMNI Hourly Data Set [Data set]. NASA Space Physics Data Facility. **https://doi.org/10.48322/1shr-ht18**.

Rönnmark, K., Christiansen, P. Dayside electron cyclotron harmonic emissions. *Nature* **294,** 335–338 (1981). https://doi.org/10.1038/294335a0

Sandel, B., Goldstein, J., Gallagher, D. *et al.* Extreme Ultraviolet Imager Observations of the Structure and Dynamics of the Plasmasphere. *Space Science Reviews* **109,** 25–46 (2003). https://doi.org/10.1023/B:SPAC.0000007511.47727.5b

Sentman, D.D., Frank, L.A., Gurnett, D.A., Kurth, W.S. and Kennel, C.F. (1979), Electron distribution functions associated with electrostatic emissions in the dayside magnetosphere. Geophys. Res. Lett., 6: 781-784. https://doi.org/10.1029/GL006i010p00781

Xiao, F., Zhou, Q., Su, Z., He, Z., Yang, C., Liu, S., He, Y., and Gao, Z. (2016), Explaining occurrences of auroral kilometric radiation in Van Allen radiation belts, *Geophys. Res. Lett.*, 43, 11,971– 11,978, doi:10.1002/2016GL071728.

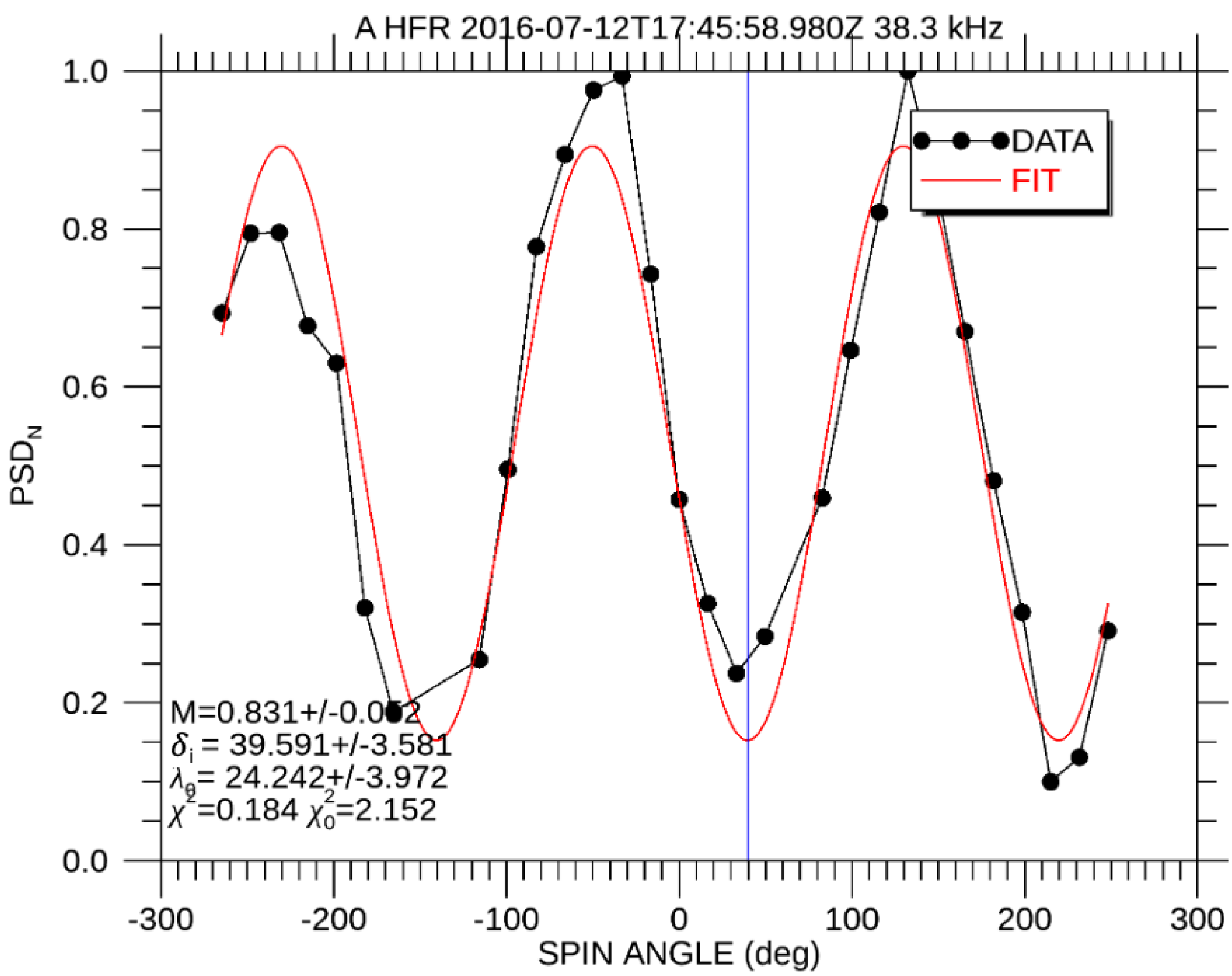

Figure 1. An example fit of the spin modulation curve for the frequency channel at 38.3 kHz. The fit parameters and their uncertainties are listed. The power spectral density PSD_N is normalized to the peak value. χ^2 is the chi squared of the spin modulation curve fit and χ^2_0 is the chi squared for a constant offset fit.

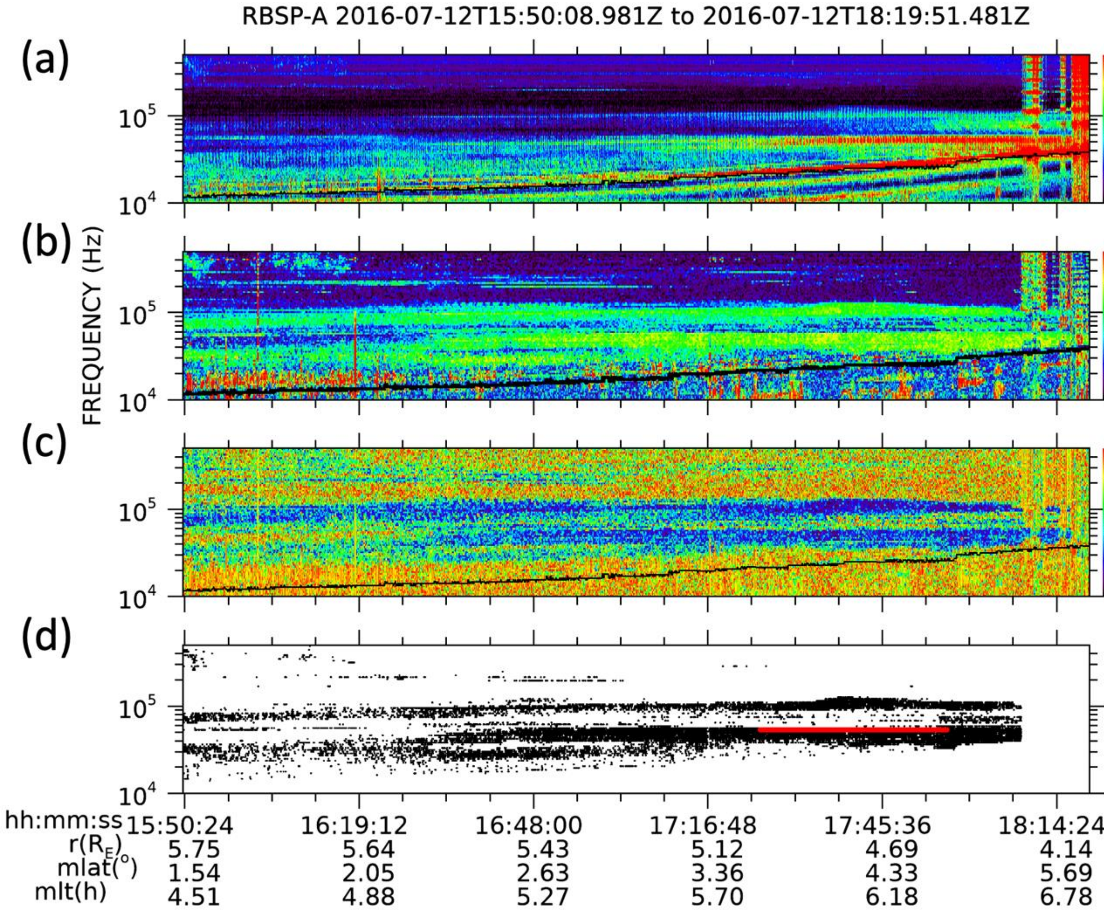

Figure 2. Escaping continuum example. Panel (a) spectrogram of the phase space density, (b) spectrogram of the modulation index *m*, (c) χ^2/χ^2_0 ratio, and (d) selections. The black line is the UHF derived plasma frequency. The red lines in panel (d) correspond to selections at 53.6 kHz between 4.5 and 5 R_E used in Figure 8, 9 & 10.

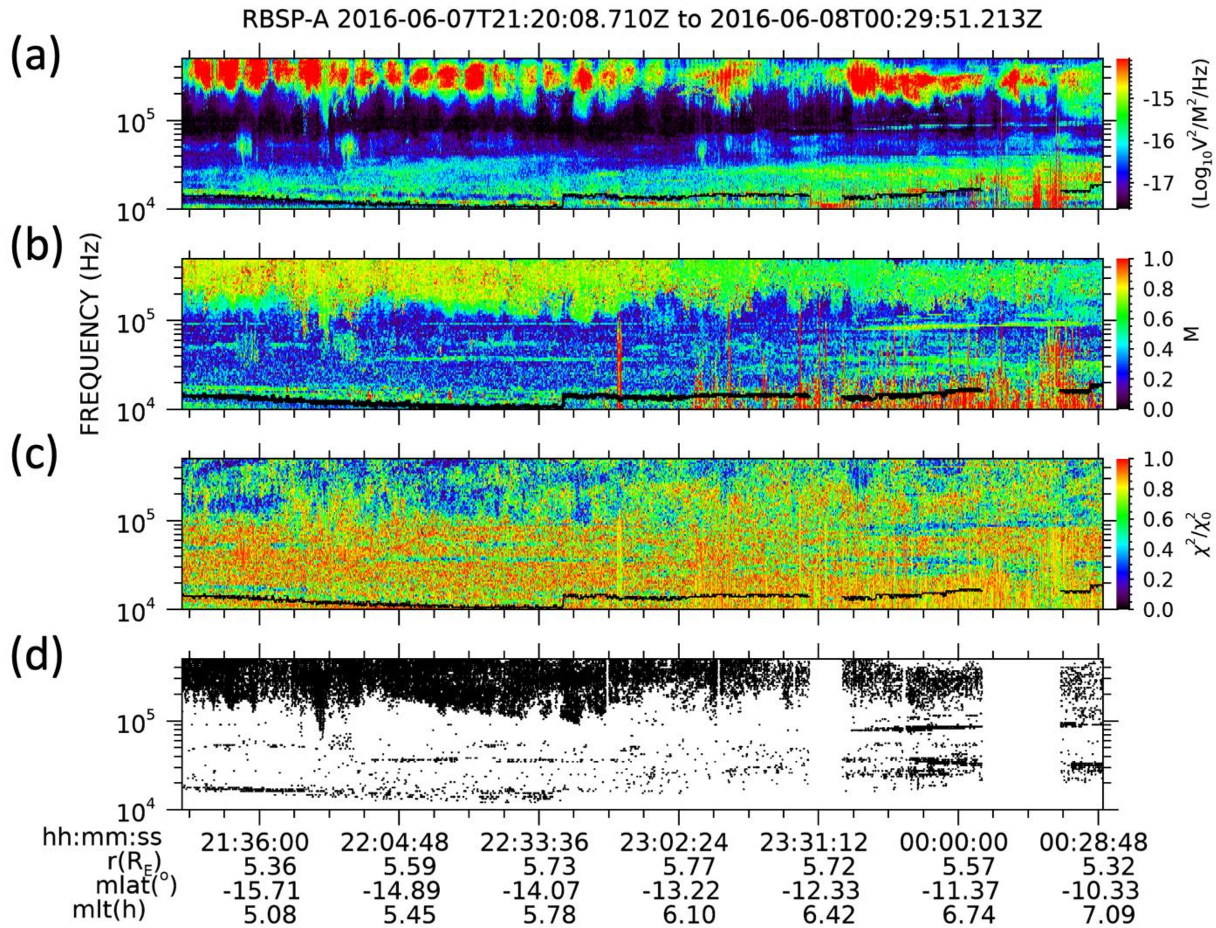

Figure 3. Emissions at *f* from 200 to 500 kHz are interpreted to be L-O mode AKR a source of contamination of the selections above 100 kHz. Panel (a) spectrogram of the phase space density, (b) spectrogram of the modulation index *m*, (c) χ^2/χ^2_0 ratio, and (d) selections. The black line is the UHF derived plasma frequency.

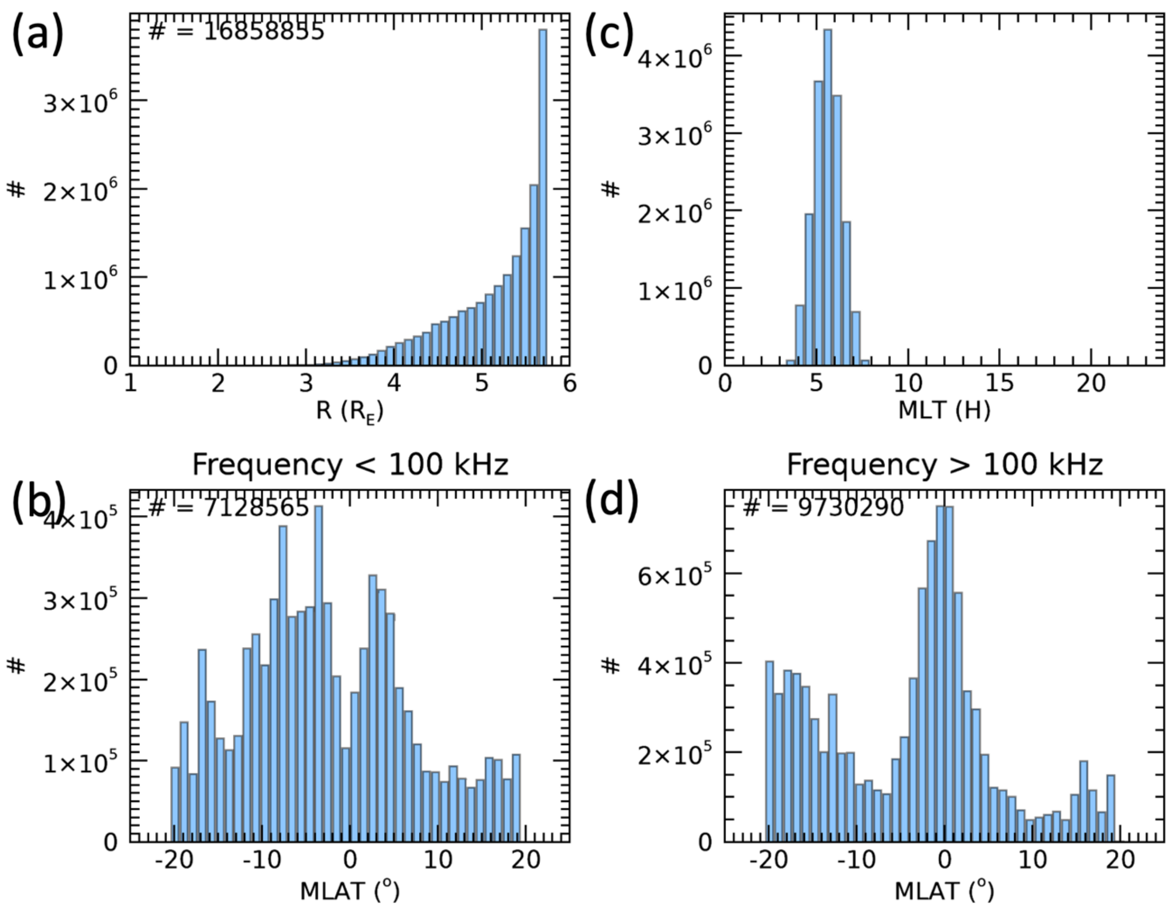

Figure 4. Histogram of the selections: (a) radial distance, (c) Magnetic local time, and magnetic latitude for (b) $f < 100$ kHz and (d) $f > 100$ kHz.

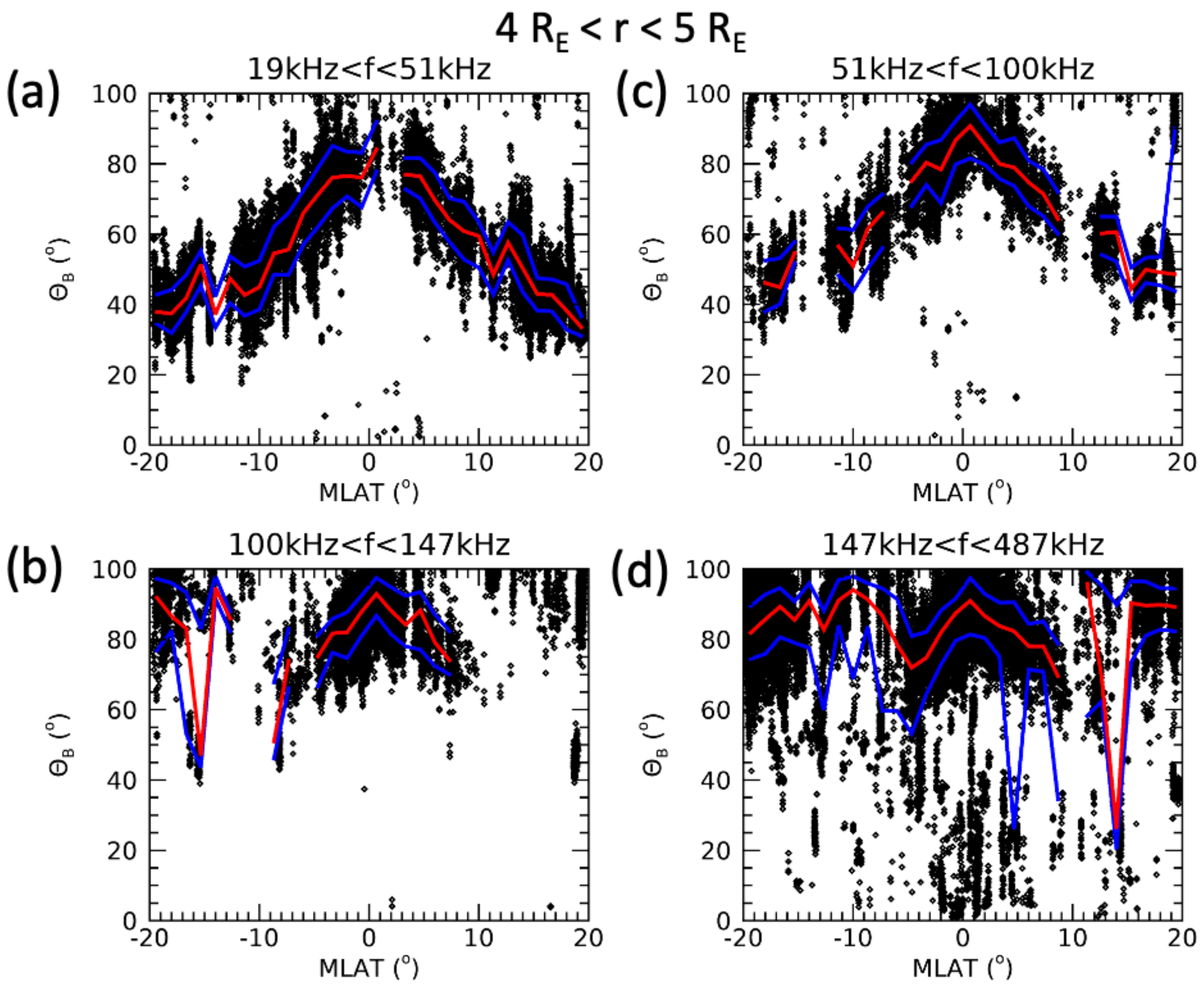

Figure 5. Scatter plots for 4 R_E < r < 5 R_E of beaming angle θ_B versus magnetic latitude. For (a) f <50 kHz, (b) 50kHz < f < 100kHz, (c) 100kHz < f < 150kHz , and (d) 150kHz < f < 500kHz. The curves are the running percentiles, blue 50th (median), red 16th and 84th percentiles.

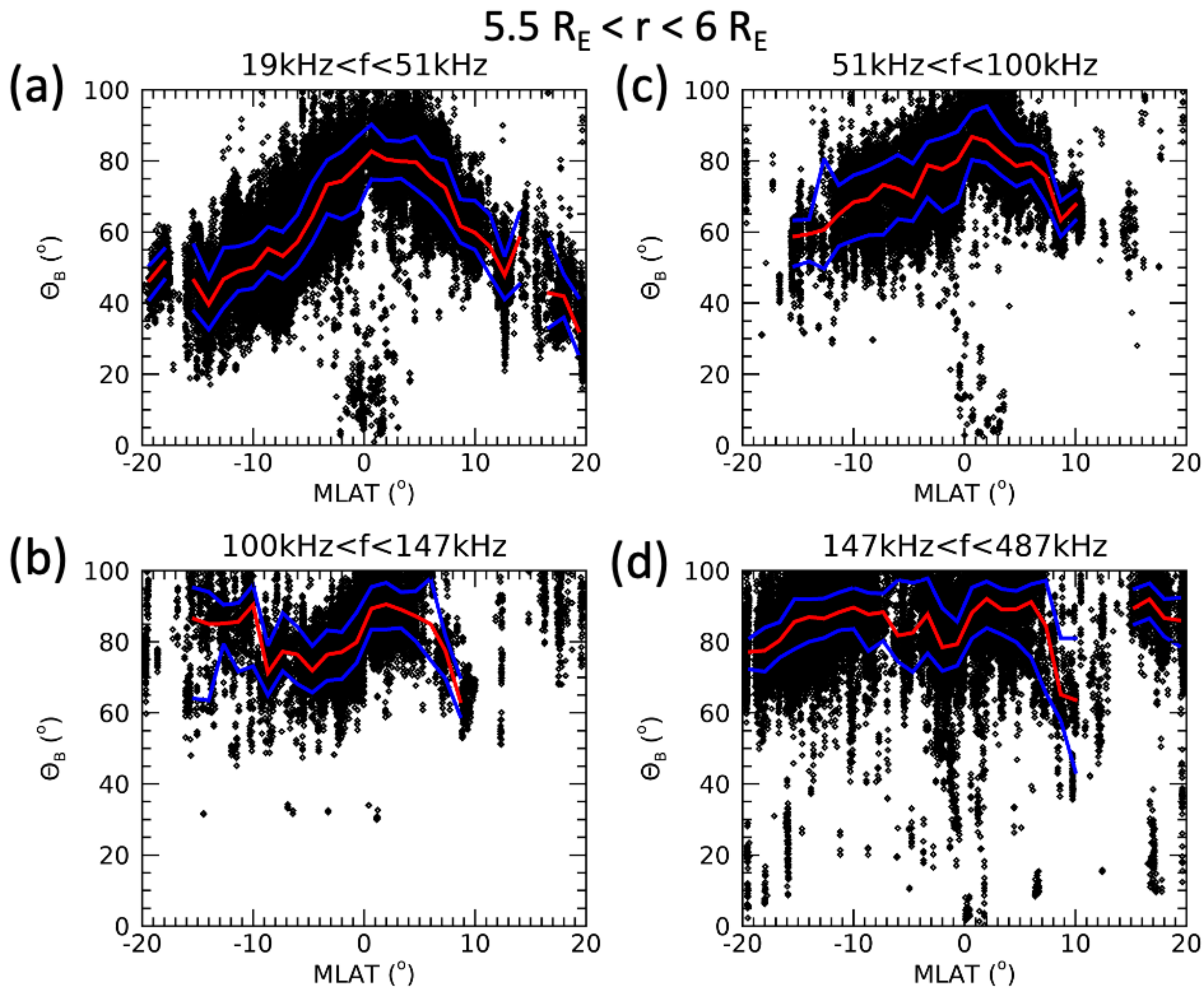

Figure 6. Scatter plots for r >5.5 R_E of beaming angle Θ_B versus magnetic latitude. For (a) f <50 kHz, (b) 50kHz < f < 100kHz, (c) 100kHz < f < 150kHz , and (d) 150kHz < f < 500kHz. The curves are the running percentiles, blue 50th (median), red 16th and 84th percentiles.

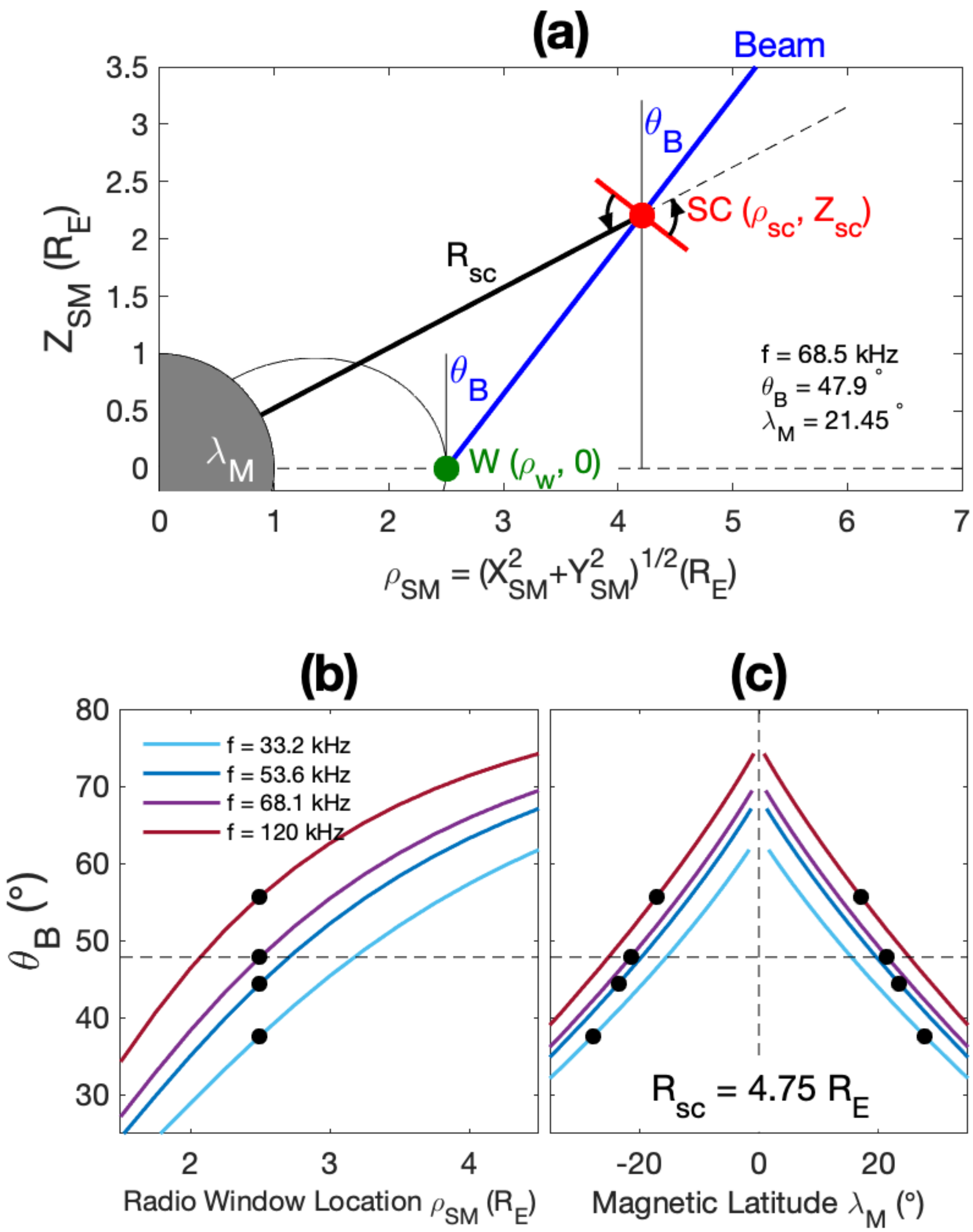

Figure 7 (a) Illustration of the meridian beaming geometry. The blue line represents the NTC beam emitted at the radio window *W* (green circle). The satellite *SC* (red circle) is at a radial distance R_{SC} and magnetic latitude λ_M. Θ_B is measured from background magnetic field $\boldsymbol{B}$ ($\boldsymbol{B} \parallel$ $\mathbf{Z_{SM}}$) at *W*. (b) Θ_B as *W* changes with radial distance. Θ_B (black circles) when *W* is located at L=2.5R_E (i.e., the plasmapause is at 2.5R_E). (c) The predicted Θ_B for R_{SC} at 4.75 R_E versus λ_M for plasmapause locations varying between 1.5 to 4.75 R_E. For example, at f = 68.1 kHz emission from a plasmapause located at 2.5R_E with a θ_B of 47.9° (b) will be observed by a spacecraft at 4.75R_E at λ_M of ±21.45°, indicated by the dashed horizontal line in panels (b) and (c).

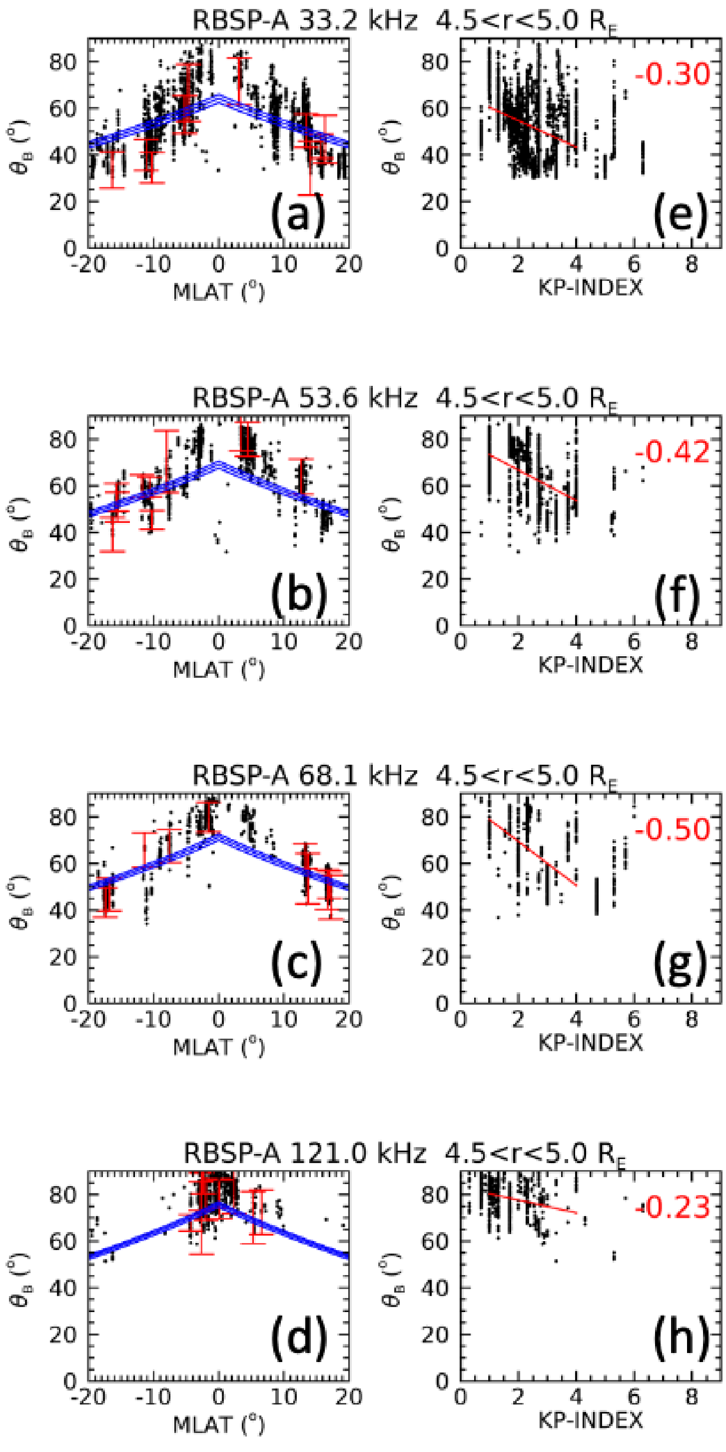

Figure 8. Scatter plots for r between 4.5 and 5.0 R_E; beaming angle (a-d) Θ_B versus magnetic latitude and (e-i) K_p index, for frequencies of 33.2 kHz, 53.6 kHz, 68.1 kHz, and 121.0 kHz. The

blue curves (a-d) are the statistical LMCT theory curves for r of 4.5, 4.75, and 5.0 R_E. Error bars indicated by red brackets are plotted for 10 randomly selected measurements. In (e-h) the red lines are linear fits, and the red numbers are the non-linear Spearman correlation coefficients, which lie in the (e) weak, (f) moderate, (g) moderate, and (h) poor range.

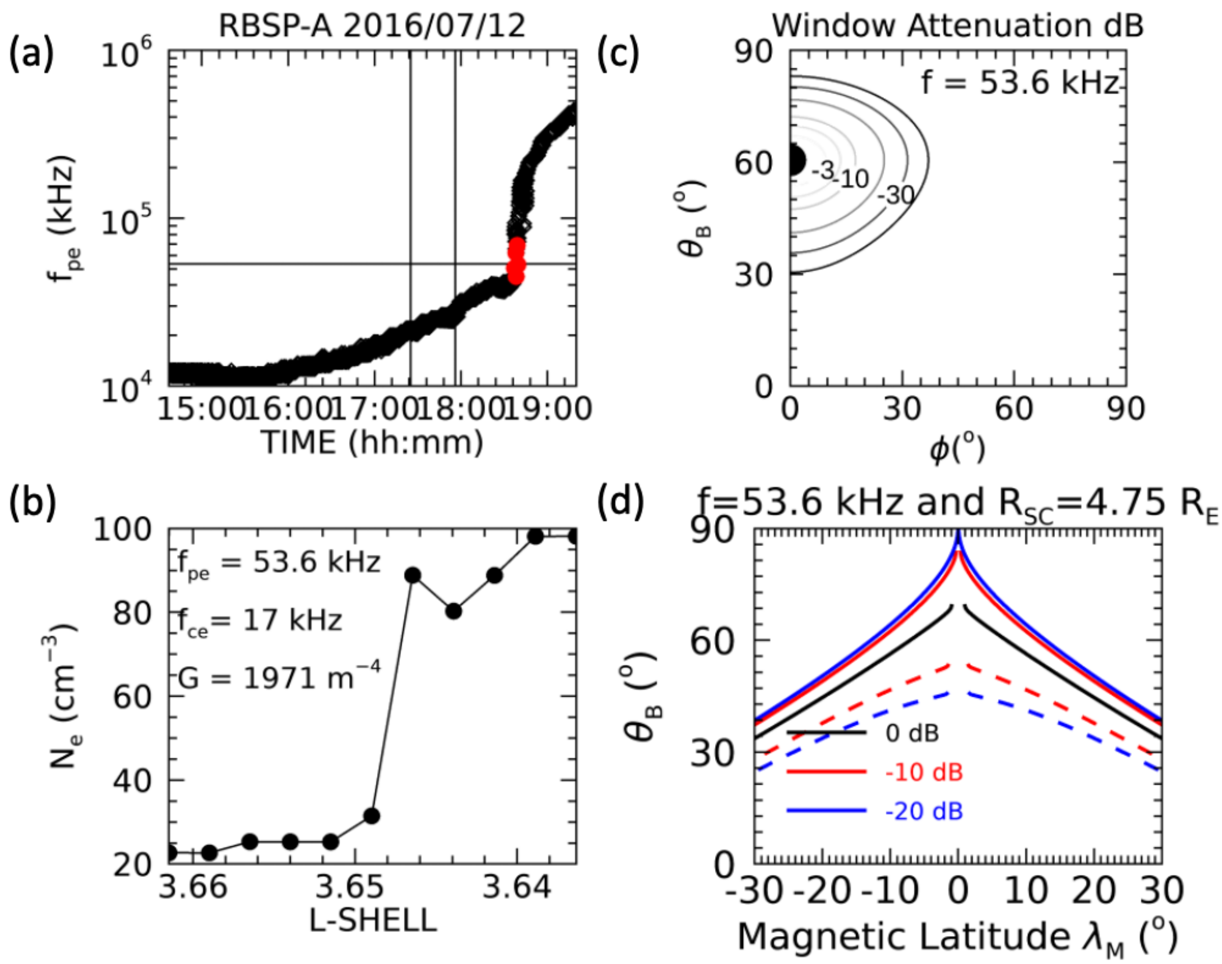

Figure 9 (a) The nearest plasmapause is indicated (red dots), where f = 53.6 kHz intersects f_{pe} for the NTC emissions shown in Figure 2. The vertical lines are where the orbit goes from 5.0 to 4.5 RE. (b) The intersection point is at L=3.65, magnetic latitude = 7.18°, MLT=7 h, the radial electron density gradient is G is -1971 m^{-4}. (b) For f=53.6 kHz the radio window attenuation in decibels is shown as a function θ_B and ϕ (azimuthal angle measured from the plasmapause). The window center is indicated by the black dot where the attenuation is 0 dB (100% transmission). (c) The inverted V pattern is shown for f = 53.6 kHz using same assumptions as in Figure 7, but attenuation of emissions that are off centered are included. Black curve is at the window center, same as that of Figure 7, the red (blue) curves are for emissions attenuated by -10 dB (-20 dB).

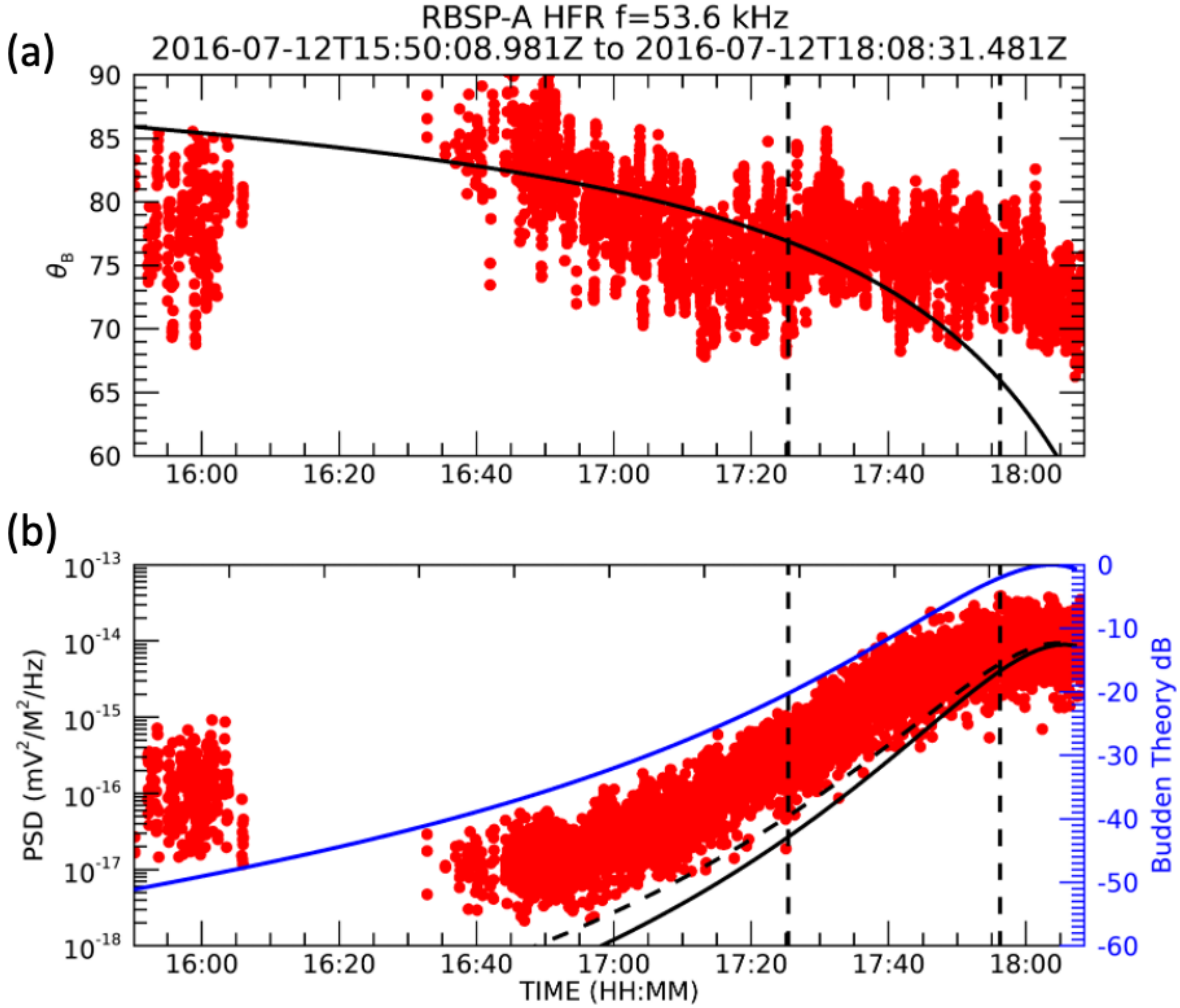

Figure 10. At a frequency of 53.6 kHz for the orbit segment shown in Figure 2 a scatter plot (red circles) is shown of (a) signal measured θ_B and (b) Power Spectral Density versus time. The black curve in (a) is θ_B based on the spacecraft location and the estimated window location, and the blue curve for (b) is the attenuation of the signal in decibels given by equation (23) of Budden (1980) (right y-axis) for the curve in (a). The dashed and dotted lines are the PSD proportional to the power of the attenuation times $1/\rho_w^2$ and $1/\rho_w$ respectively. The two vertical dashed lines are where the orbit goes from 5.0 to 4.5 REcs.

Figure 1.

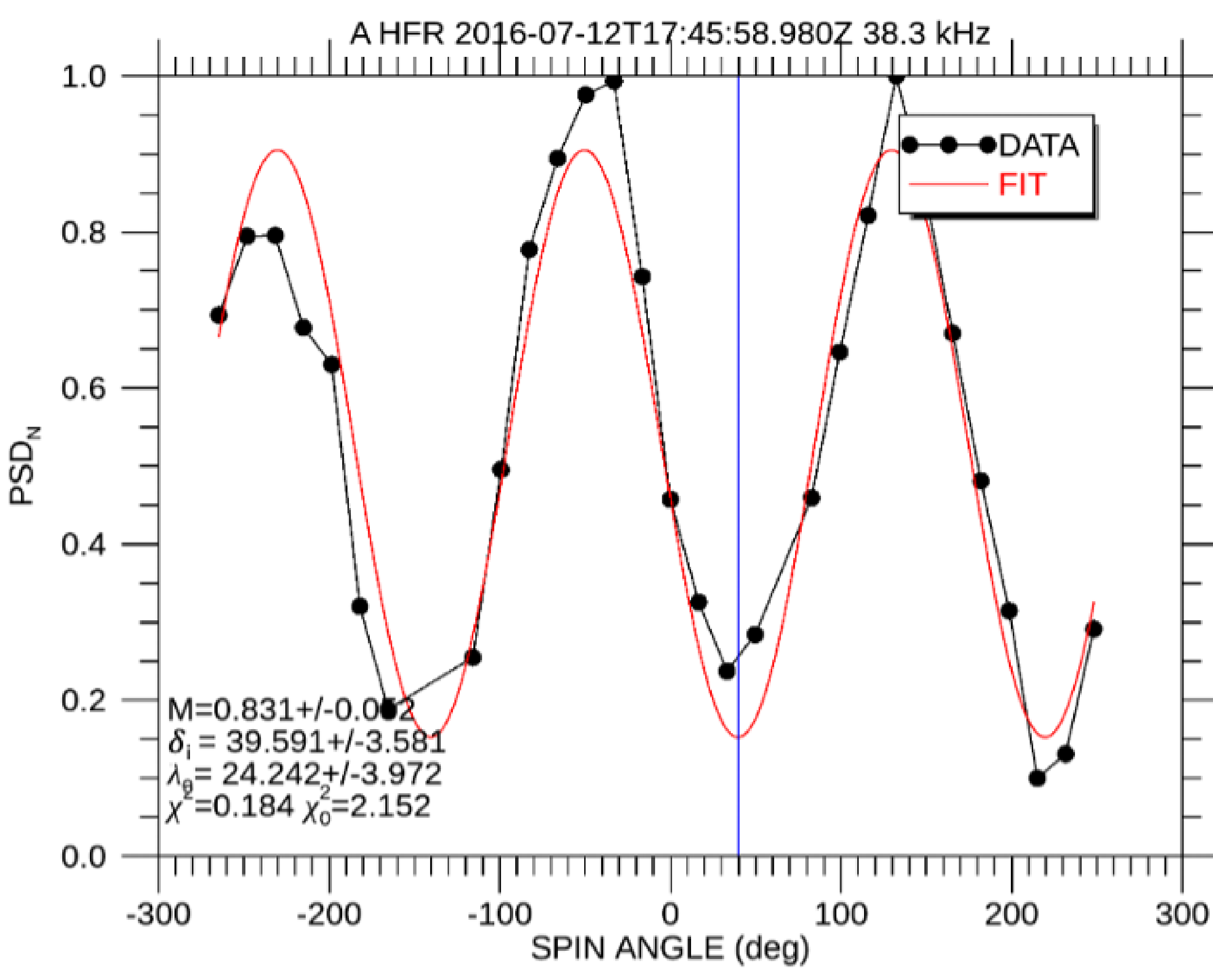

A HFR 2016-07-12T17:45:58.980Z 38.3 kHz
DATA
FIT
M=0.831+/-0.082
δ_i = 39.591+/-3.581
λ_g= 24.242+/-3.972
χ^2=0.184 χ_0^2=2.152
PSD_N
SPIN ANGLE (deg)
-300
-200
-100
0
100
200
300
0.0
0.2
0.4
0.6
0.8
1.0

Figure 2.

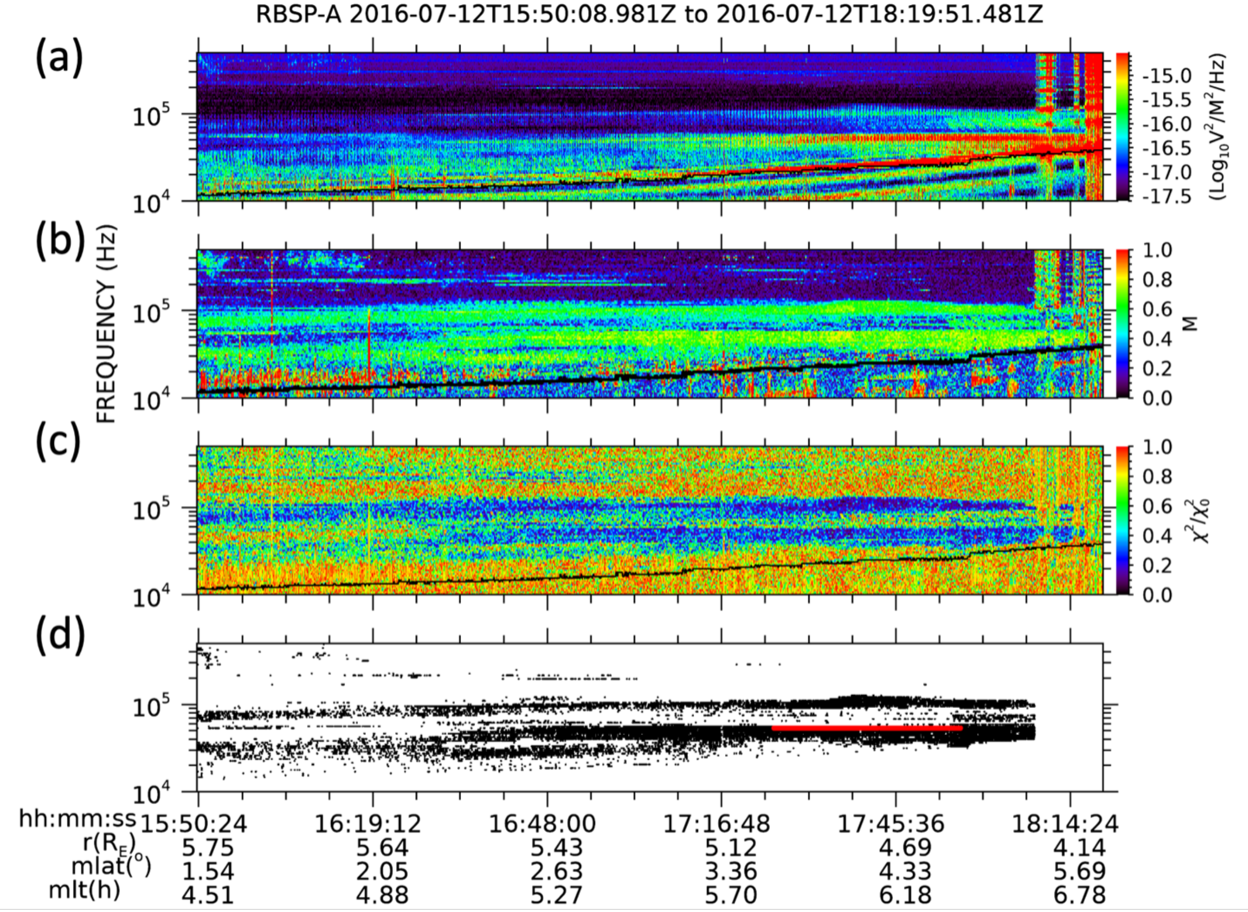

RBSP-A 2016-07-12T15:50:08.981Z to 2016-07-12T18:19:51.481Z
(a)
(b)
(c)
(d)
FREQUENCY (Hz)
10^5
10^4
-15.0
-15.5
-16.0
-16.5
-17.0
-17.5
$(Log_{10}V^2/M^2/Hz)$
1.0
0.8
0.6
0.4
0.2
0.0
M
χ^2/χ_0^2
hh:mm:ss 15:50:24 16:19:12 16:48:00 17:16:48 17:45:36 18:14:24
$r(R_E)$ 5.75 5.64 5.43 5.12 4.69 4.14
mlat(°) 1.54 2.05 2.63 3.36 4.33 5.69
mlt(h) 4.51 4.88 5.27 5.70 6.18 6.78

Figure 3.

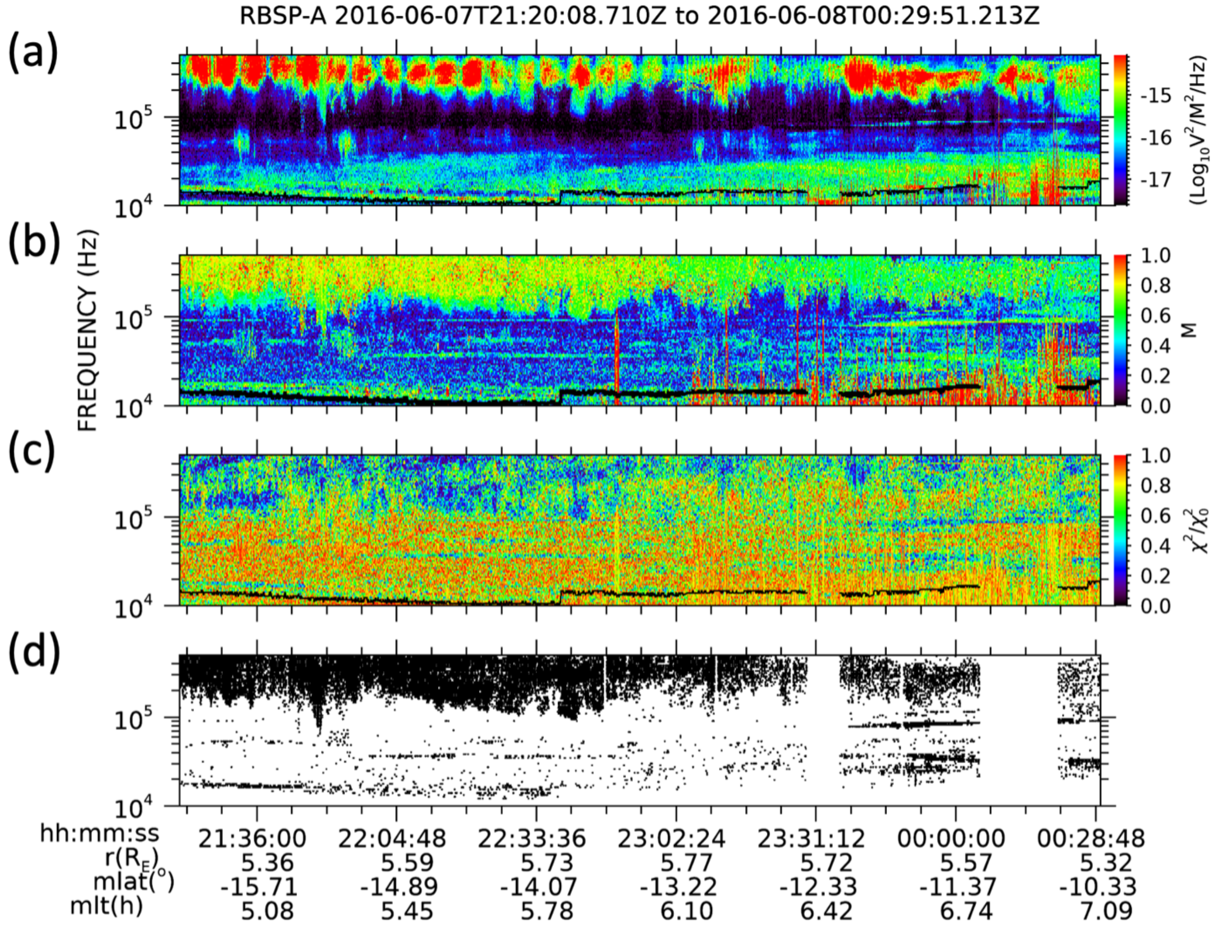

RBSP-A 2016-06-07T21:20:08.710Z to 2016-06-08T00:29:51.213Z
(a)
(b)
(c)
(d)
FREQUENCY (Hz)
10^5
10^4
$(\mathrm{Log}_{10}\mathrm{V}^2/\mathrm{M}^2/\mathrm{Hz})$
-15
-16
-17
M
χ^2/χ^2_0
0.0
0.2
0.4
0.6
0.8
1.0
hh:mm:ss 21:36:00 22:04:48 22:33:36 23:02:24 23:31:12 00:00:00 00:28:48
$r(R_E)$ 5.36 5.59 5.73 5.77 5.72 5.57 5.32
mlat(°) -15.71 -14.89 -14.07 -13.22 -12.33 -11.37 -10.33
mlt(h) 5.08 5.45 5.78 6.10 6.42 6.74 7.09

Figure 4.

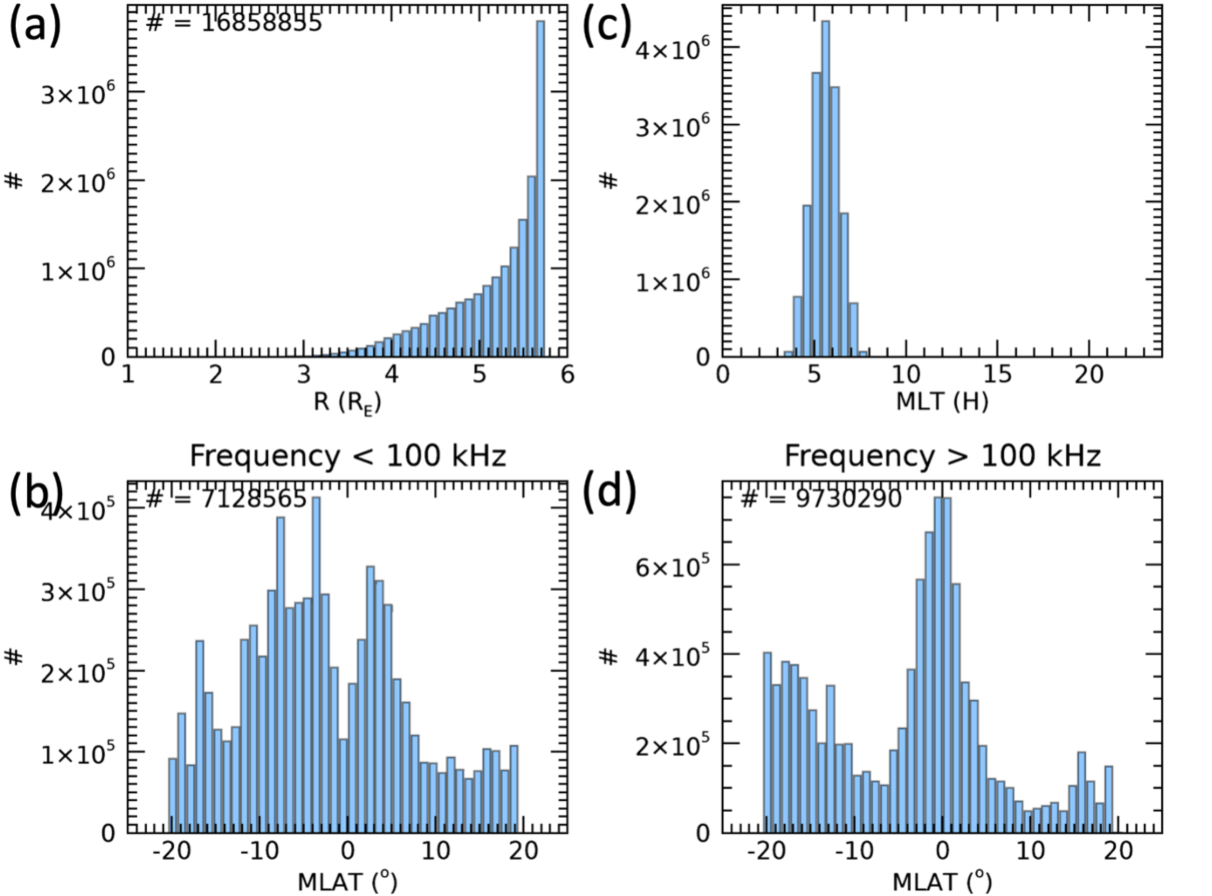

(a)
= 16858855
3×10^6
2×10^6
1×10^6
0
#
1
2
3
4
5
6
R (R_E)
(c)
4×10^6
3×10^6
2×10^6
1×10^6
0
#
0
5
10
15
20
MLT (H)
Frequency < 100 kHz
(b)
= 7128565
4×10^5
3×10^5
2×10^5
1×10^5
0
#
-20
-10
0
10
20
MLAT (°)
Frequency > 100 kHz
(d)
= 9730290
6×10^5
4×10^5
2×10^5
0
#
-20
-10
0
10
20
MLAT (°)

Figure 5.

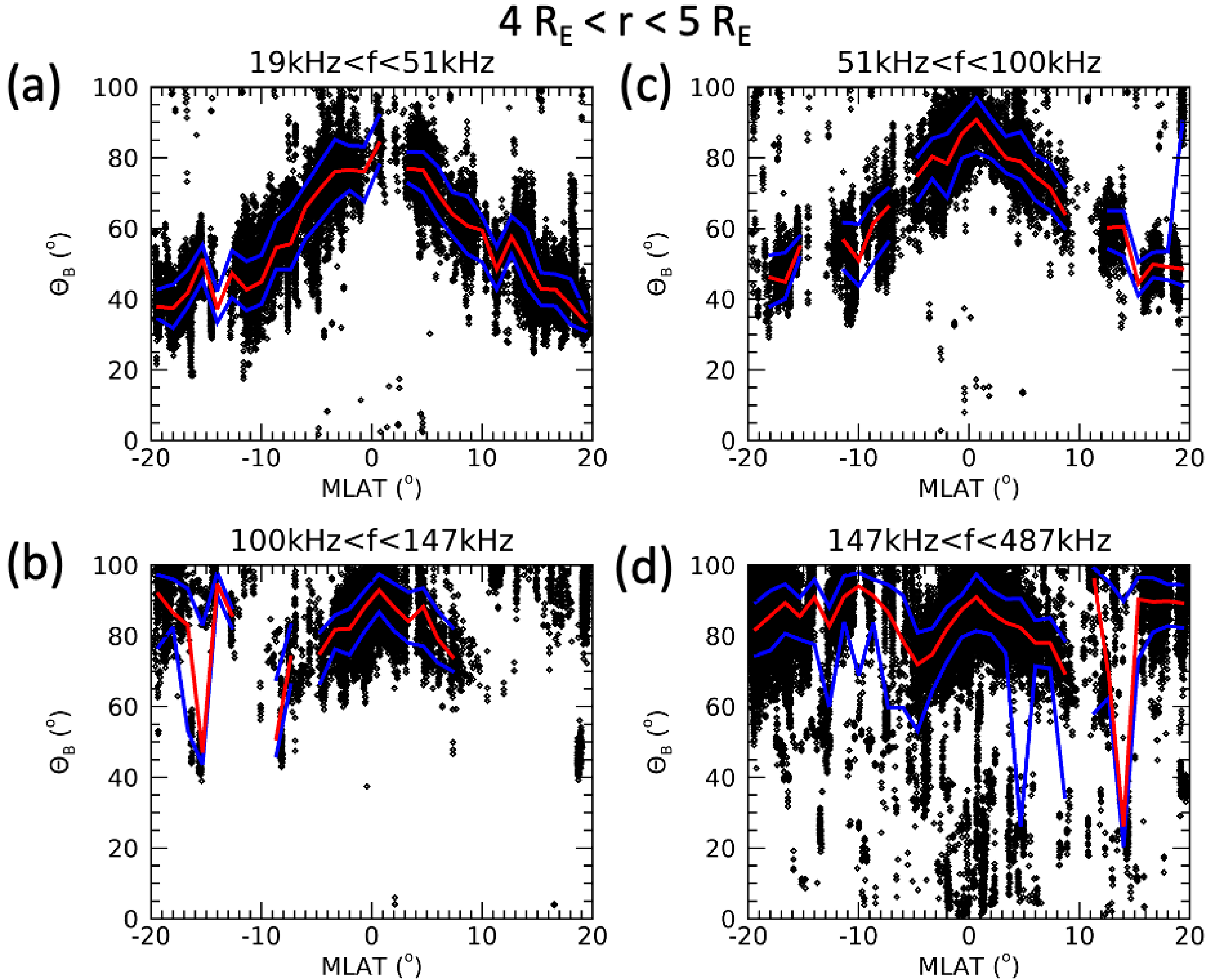

4 R_E < r < 5 R_E
(a)
19kHz<f<51kHz
(c)
51kHz<f<100kHz
(b)
100kHz<f<147kHz
(d)
147kHz<f<487kHz
Θ_B (°)
MLAT (°)
100
80
60
40
20
0
-20
-10
0
10
20

Figure 6.

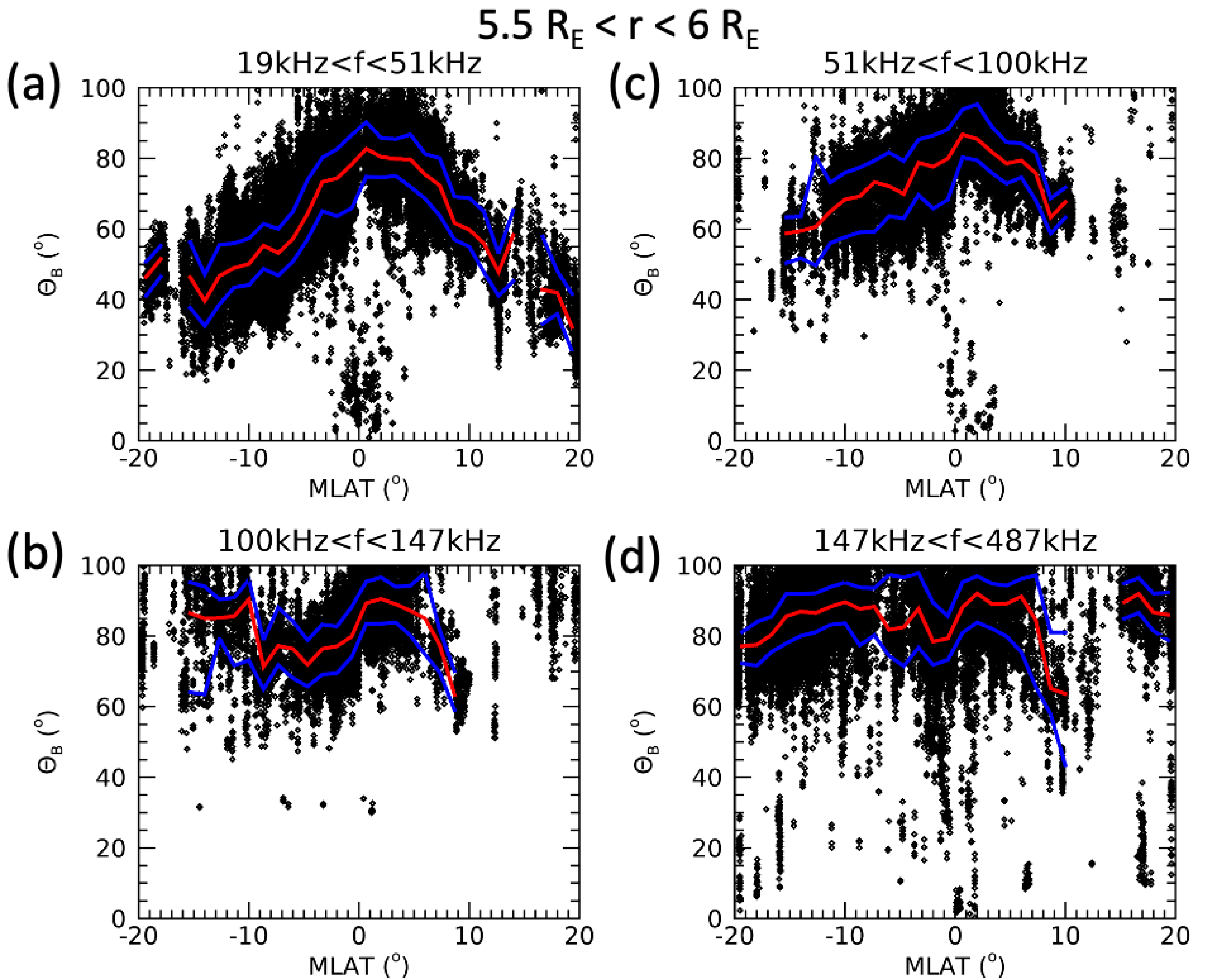

5.5 R_E < r < 6 R_E
(a)
19kHz<f<51kHz
(c)
51kHz<f<100kHz
(b)
100kHz<f<147kHz
(d)
147kHz<f<487kHz
Θ_B (°)
MLAT (°)

Figure 7.

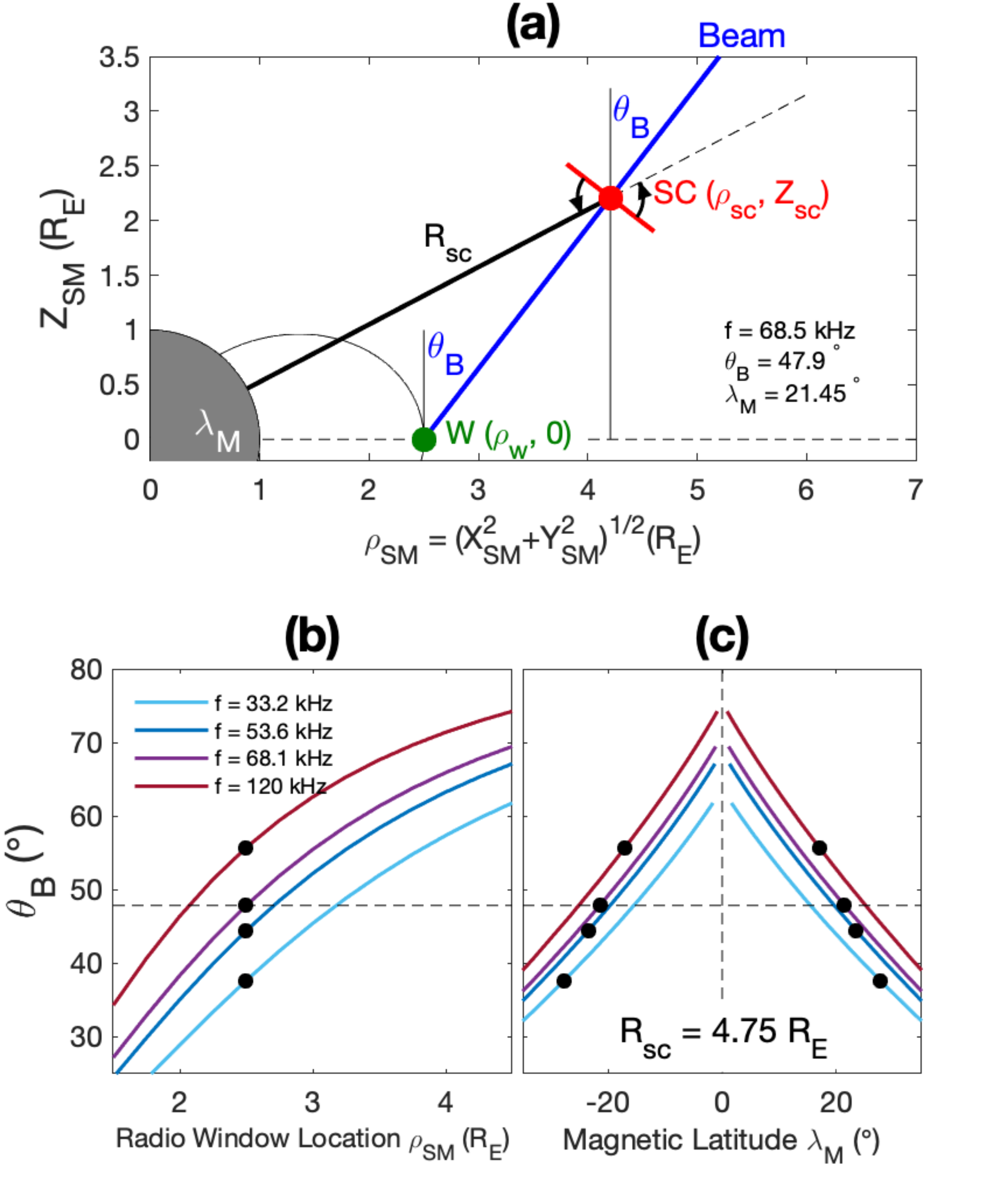

(a)
Beam
θ_B
SC (ρ_{sc}, Z_{sc})
R_{sc}
θ_B
W (ρ_w, 0)
λ_M
f = 68.5 kHz
θ_B = 47.9 °
λ_M = 21.45 °
Z_{SM} (R_E)
$\rho_{SM} = (X_{SM}^2+Y_{SM}^2)^{1/2}(R_E)$
(b)
(c)
f = 33.2 kHz
f = 53.6 kHz
f = 68.1 kHz
f = 120 kHz
θ_B (°)
R_{sc} = 4.75 R_E
Radio Window Location ρ_{SM} (R_E)
Magnetic Latitude λ_M (°)

Figure 8.

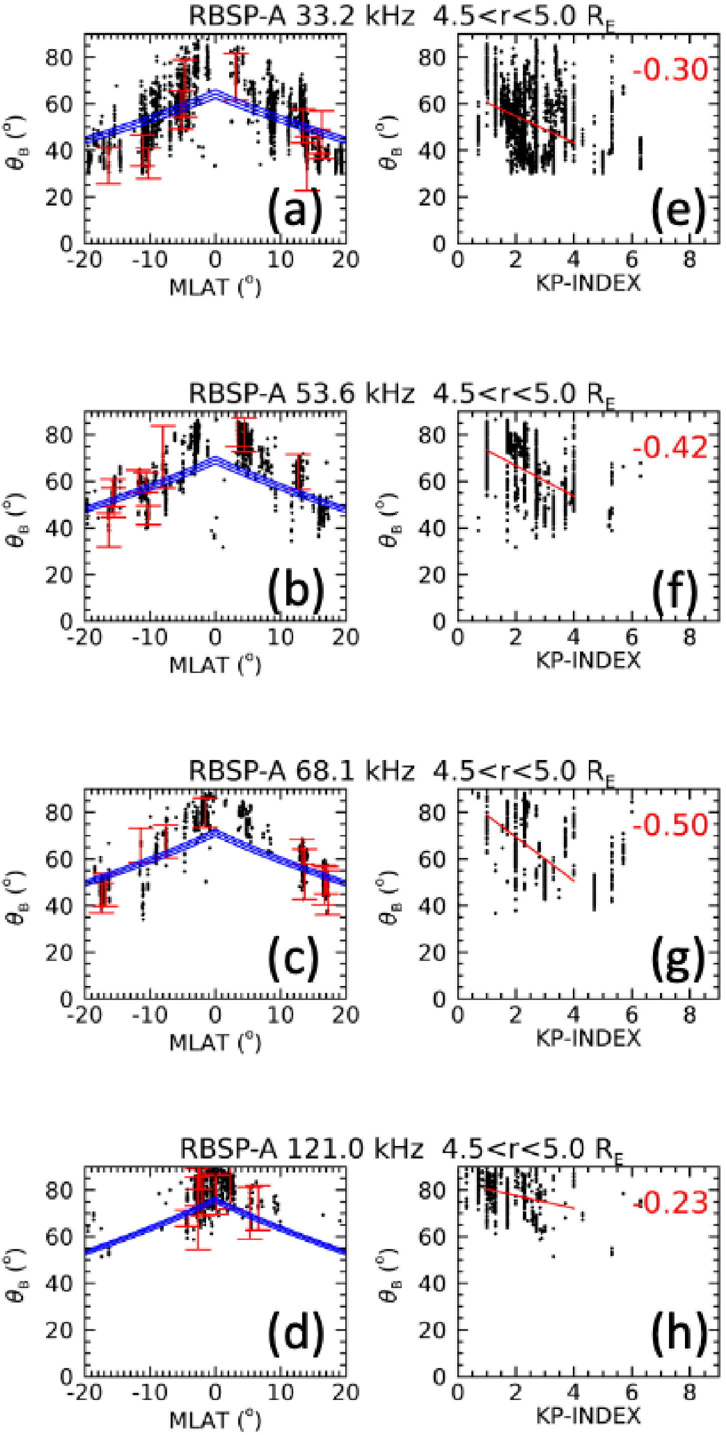

RBSP-A 33.2 kHz 4.5<r<5.0 R$_E$
(a)
(e)
-0.30
RBSP-A 53.6 kHz 4.5<r<5.0 R$_E$
(b)
(f)
-0.42
RBSP-A 68.1 kHz 4.5<r<5.0 R$_E$
(c)
(g)
-0.50
RBSP-A 121.0 kHz 4.5<r<5.0 R$_E$
(d)
(h)
-0.23
θ_B (°)
MLAT (°)
KP-INDEX

Figure 9.

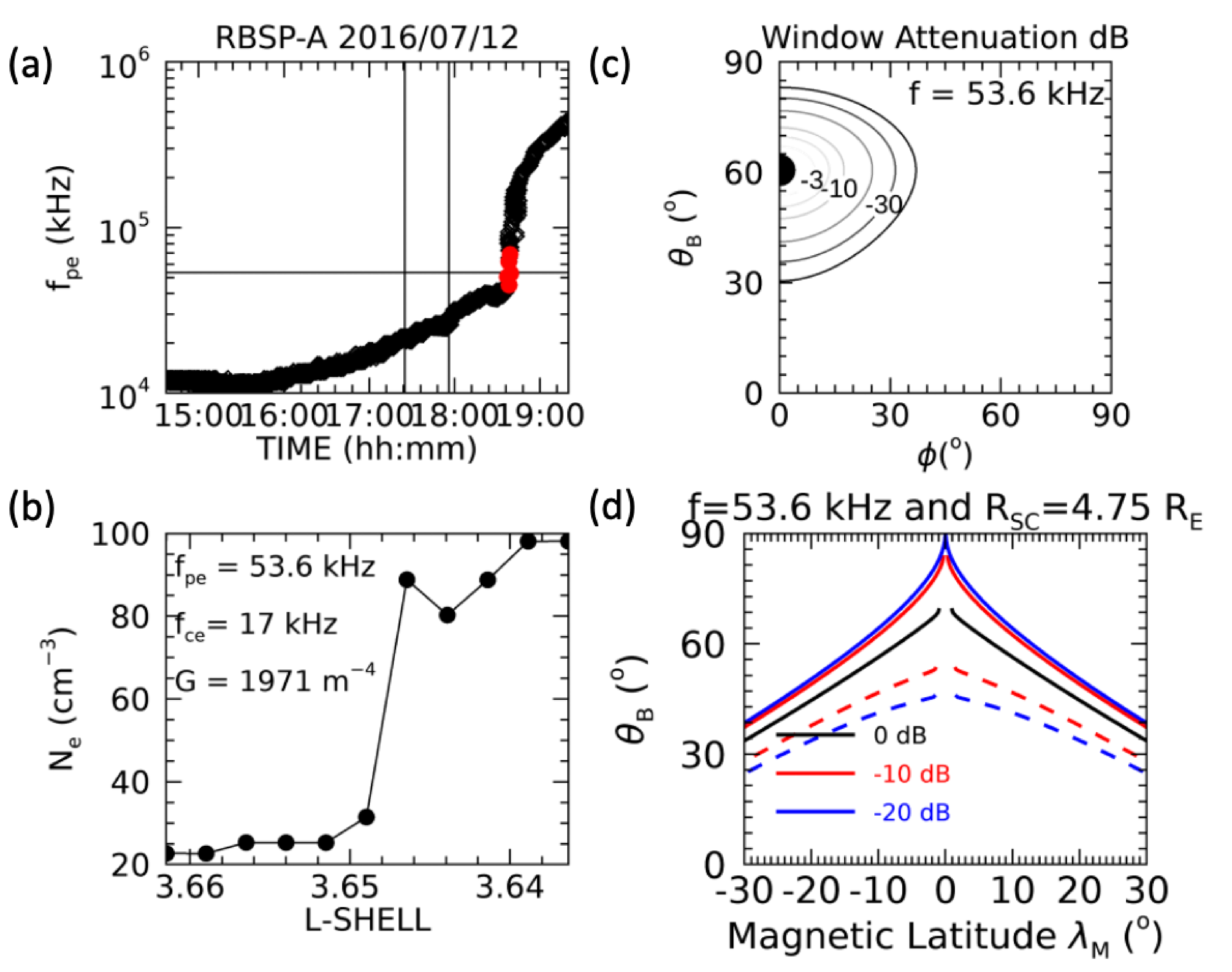

(a)
RBSP-A 2016/07/12
f_{pe} (kHz)
10^6
10^5
10^4
15:00 16:00 17:00 18:00 19:00
TIME (hh:mm)
(c)
Window Attenuation dB
f = 53.6 kHz
-3
-10
-30
θ_B (°)
ϕ(°)
(b)
f_{pe} = 53.6 kHz
f_{ce}= 17 kHz
G = 1971 m^{-4}
N_e (cm^{-3})
L-SHELL
3.66 3.65 3.64
(d)
f=53.6 kHz and R_{SC}=4.75 R_E
0 dB
-10 dB
-20 dB
θ_B (°)
Magnetic Latitude λ_M (°)

Figure 10.

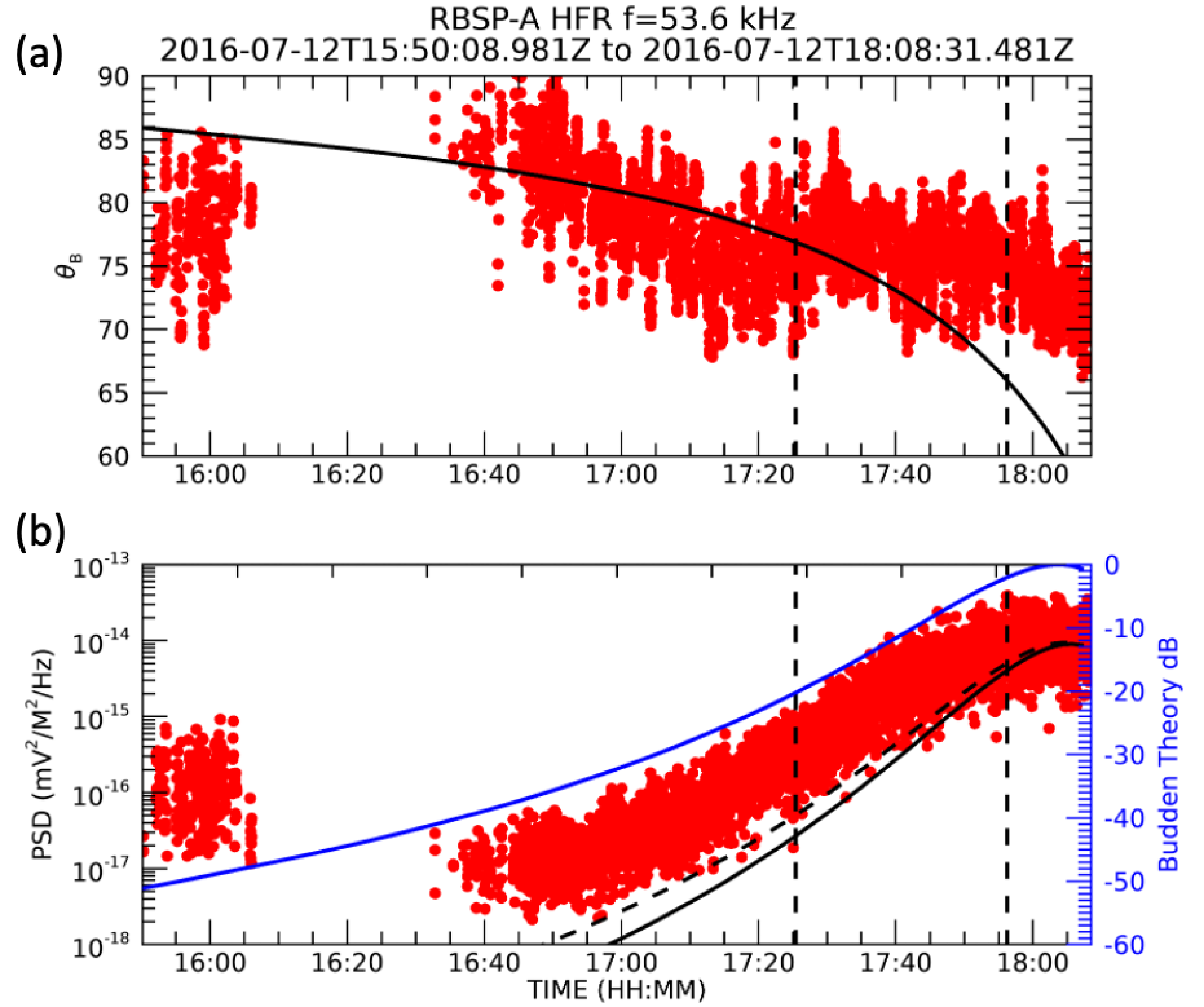
RBSP-A HFR f=53.6 kHz
2016-07-12T15:50:08.981Z to 2016-07-12T18:08:31.481Z
(a)
90
85
80
75
70
65
60
θ_B
16:00
16:20
16:40
17:00
17:20
17:40
18:00
(b)
10^{-13}
10^{-14}
10^{-15}
10^{-16}
10^{-17}
10^{-18}
PSD ($mV^2/M^2/Hz$)
0
-10
-20
-30
-40
-50
-60
Budden Theory dB
TIME (HH:MM)